https://doi.org/10.1016/j.conbuildmat.2021.124240

Stochastic Three-dimensional Reconstruction of Realistic Stone-based Materials with Controllable Stone Inclusion Geometries

Wang Xiang[1,2], Yin Zhen-yu[2], Zhang Jun-qi[2,3], Xiong Hao[1*], Su Dong[1]

Abstract: Stone-based materials are heterogeneous construction materials that mainly consist of coarse stones and fine matrix. When using the numerical simulation tools (FEM, DEM, FDEM) to study the mechanical properties of the tone-based materials, the irregular stone-inclusion geometries cannot be neglected. This main objective of this study is to generate three-dimensional models of realistic stone-based materials with controllable stone-inclusion geometries. To achieve this goal, two major methodologies are adopted: (1) the Spherical Harmonic transform (SHT) method and inverse Monte-Carlo (IMC) algorithm are employed to randomly generate the 3D particle model of irregular stones with controllable geometries at three different shape scales, including form, roundness and roughness, and (2) based on the Spherical Harmonic function, an innovative overlapping detection algorithm is proposed to facilitate the rapid allocation of the 3D SHT-based particles. The proposed algorithm can quantitatively control the statistics of several geometrical features of the generated stone-based materials in an efficient and precise manner. Finally, the application of the proposed approach is demonstrated through the discrete modelling of stone-based materials with different stone contents and stone shapes. The proposed study has the significance to pave a viable pathway for stochastic modelling of stone-based materials pertaining to various construction and manufacture processes.

Keywords: Stone-based material; Stone inclusion; Stochastic model; Realistic stone shape; Spherical Harmonic; Overlapping detection; DEM simulation

1 Introduction

Stone-based materials are very complicated and heterogeneous construction materials with a stone-in-matrix texture. They are either widely distributed in the nature or massively produced in the industry and usually described as a multi-phase material that mainly consist of coarse stones and fine matrix [1-3]. Typical stone-based materials include gravel deposits [7], cement/asphalt concrete [5-6], rock-soil mixtures [7], sandy cobbles [8-9], fouled ballast [10-12], etc. Due to the variation of the internal structure and components properties, the physical and mechanical characteristics of stone-based materials are quite distinctive from the homogeneous construction materials. Especially, the stone-inclusion features, e.g., stone content [13], stone size distributions [14], stone particle shapes [15], and stone orientations [16], are essential factors influencing the mechanical properties of stone-based materials. Due to the high contrast of mechanical features between fine matrix and coarse stones, the heterogeneity and discontinuity of the stone-based materials are easy to cause failure of the related engineering structures [17]. Therefore, it is of great significance to study how the stone-inclusion features affect the mechanical and physical characteristics of stone-based materials.

In the past few decades, researchers have conducted massive experimental tests, e.g., the uniaxial or triaxial compression tests [18-21], shear tests [22], ultrasonic tests [23],and acoustic emission (AE) test [24] to investigate the mechanical properties of stone-based materials. However, the preparation of representative and undisturbed specimen of stone-based material can be rather difficult and exhausting [25], which may contribute to unexpected errors to tests results. It is also known that the researchers can hardly quantify the stone-inclusion feature effects through only the laboratory experiments due to the dimension variability and shape complexity [2]. Nevertheless, the meso-mechanical behaviors and internal interactions of stone-based material can not be observed through the traditional experimental apparatus.

To overcome the limitations encountered in the experiment, the numerical method emerged as an effective and convenient tool to study the mechanical behaviors of study stone-based materials. Zhang S et al. [26] employed an equivalent ellipse to represent the rock stone with

the same area and generated series of numerical specimens, following the statistical characterization of the mesostructures of stone-based materials on site. The simulation results indicate that compression strength fluctuated differently against the stone proportions on the various model scales, which contradicts the previous scale-independent assumption [22, 27]. Similarly, Emad Khorasani et al [28] chose ellipsoid to present the stone and conducted both physical and numerical study on slopes at a laboratory scale. Meng Q X [29] and Xu Wenjie [30, 31] chose irregular polygons and polyhedrons to represent the 2D and 3D rock stone, respectively. Both them developed codes to generate mesostructures of stone-based materials in the finite element software. They pointed out that rock stones and interface properties play vital roles in the determination of mechanical properties of stone-based materials. Chen L et al [32] developed an aggregate structure generation method based on random sequential addition, which significantly improved allocation efficiency. The developed model is able to obtain the bimrocks with a high stone proportions and the stone shape of convex polygon. However, the shapes effects can not be well considered by representing the rock stones with regular geometry, which may play critical roles in determination of mechanical properties of stone-based materials.

In the author' previous work [2], a systematic framework to generate 2D stone-based materials has been proposed. However, the algorithms were subjected to 2D condition and can not be applied to simulate realistic stone-based materials with 3D stone particle of various shapes. Thus, this paper aims to extend the previous study [2] into 3D condition by developing a stochastic method for generating a realistic 3D stone-inclusion model for the numerical simulation of stone-based materials. The inverse operation of spherical harmonic transform (SHT) is first employed to generate 3D stone particles with random and realistic morphologies. Then, the conventional 3D morphology descriptors (elongation, flatness, roundness, and roughness) are employed to analyze the morphology properties of the generated 3D stone particles. Afterward, nonlinear regression and the inverse Monte Carlo (IMC) approach are employed to determine the adopted parameters for the reconstruction of stone particles with desired morphology features. Then, the unique overlapping detection algorithm is developed to

achieve the random and quick allocation of the generated 3D SHT-based stone particles, considering the stone contents, stone size distributions, and stone orientations. Lastly, several examples are demonstrated to illustrate the capability of the proposed method. The results prove that the proposed method can reconstruct a synthetic complex 3D numerical model of realistic stone-based materials with the desired stone-inclusion features both quantitatively and precisely.

2 Representation and characterization of stone inclusion morphology

2.1 Surface data acquisition of realistic stone inclusions

In this study, the white light scanner [33] is employed to acquire the surface data of realistic stone inclusions. The scanner is mainly composed of a turntable, shown in Fig. 1 (*a*), an image acquisition device, shown in Fig. 1 (*b*), and a computer, shown in Fig. 1 (*c*). The image acquisition device is used to capture the feature points on the stone surface and transmit them to the computer; the turntable can rotate the stone so that the image acquisition device can capture the feature points from different orientations of the stone; the function of the computer is to receive the feature points and carry out matching and reconstruction. It should be noted that when the turntable rotates for one cycle, the bottom of the particle is not collected. Therefore, it is necessary to rotate the stone, as shown in Fig. 1 (*d*), to expose their bottom, and then conduct a second scan to obtain the complete morphology information of the stone. Fig. 1 (*e*) shows the triangular mesh model of the scanned stone surface.

2.2 Spherical-harmonic-transform of the stone surface

The obtained 3D surface data of the sampled stones is common in the format of triangular meshes, which is a typical discretized 3D surface model, as shown in Fig.1 (e). The discrete vertex coordinate of the triangular mesh model determines the morphology of the stone. Since the discrete vertices of the triangular meshes are under the Cartesian coordination system, a coordination transformation process, as illustrated in Fig. 2 (*a*) is required before the data can be substituted into the spherical harmonic function.

$$r_i = \sqrt{(x_i - x_c)^2 + (y_i - y_c)^2 + (z_i - z_c)^2} \tag{1}$$

$$\theta_i = \arccos\left(\frac{z_i - z_c}{r_i}\right) \tag{2}$$

$$\varphi_i = \begin{cases} \arctan\left(\frac{y_i - y_c}{x_i - x_c}\right) + 2\pi & x \geq 0, y < 0 \\ \arctan\left(\frac{y_i - y_c}{x_i - x_c}\right) + \pi & x < 0, y < 0 \\ \arctan\left(\frac{y_i - y_c}{x_i - x_c}\right) & x \geq 0, y \geq 0 \\ \arctan\left(\frac{y_i - y_c}{x_i - x_c}\right) + \pi & x < 0, y \geq 0 \end{cases} \tag{3}$$

where x_c, y_c and z_c are the Cartesian coordinates of the particle center, x_i, y_i and z_i are the Cartesian coordinates of a random surface point P_i on the particle surface.

Once the spherical coordinates $r(\theta, \varphi)$ of a stone particle is obtained, the spherical harmonic function can then be used to process the data. The spherical harmonic function is a famous higher-dimensional analogy of the Fourier series, defined on the surface of a sphere. It is widely used in many different scientific fields, such as quantum mechanics, computer graphics, rendering lighting, and sphere mapping, etc. Based on the spherical harmonic function, we can regard the surface coordinates $r(\theta, \varphi)$ of a stone particle as the superimposition of a series of spherical harmonic basis function:

$$r(\theta, \varphi) = \sum_{n=0}^{N} \sum_{m=-n}^{n} a_n^m Y_n^m(\theta, \varphi) \tag{4}$$

where N is the total order number of the spherical harmonic basis function; $\theta \in [0, \pi]$ and $\varphi \in [0, 2\pi]$; $Y_n^m(\theta, \varphi)$ represents the harmonic basis function at the order n and the degree m; a_n^m is the harmonic coefficient corresponding to $Y_n^m(\theta, \varphi)$; a group of N order harmonics contains $(N+1)^2$ number of a_n^m and $Y_n^m(\theta, \varphi)$. The basic function $Y_n^m(\theta, \varphi)$ is defined as:

$$Y_n^m(\theta, \varphi) = \sqrt{\frac{(2n+1)(n-|m|)!}{4\pi(n+|m|)!}} P_n^m(\cos\theta) e^{im\varphi} \tag{5}$$

where $P_n^m(x)$ is the related Legendre polynomials:

$$P_n^m(x) = (-1)^{|m|} \cdot (1-x^2)^{\frac{|m|}{2}} \cdot \frac{d^{|m|}P_n(x)}{dx^{|m|}} \tag{6}$$

where $P_n(x)$ is the n order Legendre polynomials:

$$P_n\ (x) = \frac{1}{2^n n!} \frac{d^n[(x^2-1)^n]}{dx^n} \tag{7}$$

The first-order to the fourth-order of the harmonic basis function can be visualized in the polar coordinate system in Fig. 2 (*b*). It can be observed from the figure that the first-order harmonic basis function corresponds to a unit sphere in the spherical coordinate system when $n = 0$. With the order increases, there are more numbers of harmonic basis functions, which correspond to more complex particle geometries in the spherical coordinate system. Assume there are total N_P number of points on the particle surface are known. Substitute the N_P number of spherical coordinates $r(\theta, \varphi)$ into equation (2), we can obtain N_P number of linear equations:

$$\begin{cases} r_1 = \sum_{n=0}^{N} \sum_{m=-n}^{n} a_n^m Y_n^m(\theta_1, \varphi_1) \\ \vdots \\ r_i = \sum_{n=0}^{N} \sum_{m=-n}^{n} a_n^m Y_n^m(\theta_i, \varphi_i) \\ \vdots \\ r_{N_P} = \sum_{n=0}^{N} \sum_{m=-n}^{n} a_n^m Y_n^m(\theta_{N_P}, \varphi_{N_P}) \end{cases} \tag{8}$$

In equation (2), the $r_1 \sim r_{N_P}$ and $Y_n^m(\theta_1, \varphi_1) \sim Y_n^m(\theta_{N_P}, \varphi_{N_P})$ are all known while there are $(N+1)^2$ number of unknown coefficients a_n^m. When N_P is larger than $(N+1)^2$, it is possible to solve these coefficients with N_P equations through Least square estimation. During this spherical harmonic transformation process, the computational cost is proportional to the

surface points number N_P and harmonic orders number N. The example of transforming the N_P number of particle surface points into $(N+1)^2$ number of harmonic coefficients a_n^m is illustrated in Fig. 3. In this example, N_P and N are set as 8192 and 31, respectively. The results of a_n^m, as illustrated in Fig. 3, are visualized in the format of a 3D bar chart. It can be seen from the figure that, when n is small, a_n^m is significant large, while n increases, a_n^m becomes minimal.

2.3 Representation of stone surface by inverse SHT

When $(N+1)^2$ harmonic coefficients for the discrete surface points of a target particle are obtained through spherical harmonic transformation, and we can use the $(N+1)^2$ harmonic functions to represent the discretized surface points as a continuous curved closed surface. This process, namely the inverse operation of spherical harmonic transformation, is illustrated as follows:

(1) First, assume a random point P_i is on the particle surface. The polar radius r_i of point P_i can be calculated by finding the intersection between the particle surface and the unit vertex (θ_i, φ_i). When N_P number of the surface points are required, we need to determine N_P number of unit vertices uniformly surrounded the origin of the spherical coordinate system. As shown in Fig. 4, these unit vertices can be illustrated as a series of surface points equally distributed on a sphere. It should be noted that N_P could be sufficiently large if high quality of 3D triangular mesh model is required.

(2) Then, substitute (θ_i, φ_i) into equation (3) to obtain the corresponding $Y_n^m(\theta_i, \varphi_i)$. For a specific pair of n and m, the values of $a_n^m Y_n^m(\theta, \varphi)$ can be visualized through the 3D contour map, as illustrated in Fig. 5.

(3) Next, for a certain harmonic order n, superimpose $(2n+1)$ number of $a_n^m Y_n^m(\theta, \varphi)$ together, where m is the integer varying from $-n$ to n. The obtained 3D contours for the summations of $a_n^m Y_n^m(\theta, \varphi)$ at different harmonic orders are shown in Fig. 6.

(4) Repeat step (3) from $n = 1$ to $n = N$, superimpose them together to obtain the final result of $r(\theta, \varphi)$. The contour of r_i versus different (θ_i, φ_i) is illustrated in Fig. 7 (*a*).

(5) Finally, use the coordinate transform equation to obtain the Cartesian coordinates (x_i, y_i, z_i) of the particle surface. As shown in Fig. 7 (*b*), the obtained points cloud model that represents the target particle surface is thus reconstructed.

$$\begin{cases} x_i = r_i \cos\theta_i \, r_i \cos\varphi_i \\ y_i = r_i \cos\theta_i \sin\varphi_i \\ z_i = r_i \sin\theta_i \end{cases} \tag{9}$$

Since the above detailed inverse SHT process can be used to calculate the coordinates of any surface points P_i, the particle surface can thus be continuously represented by the spherical harmonic function. During the above-mentioned process, the harmonic orders N is an important parameter.

As illustrated in Fig. 8, for a specific particle, when different harmonic order N is used, the obtained points cloud model is different. If very small harmonic order N is used, the spherical harmonic function tends to represent the overall shape of the original particle surface. When N increases, the represented particle becomes more similar to the original particle, while the obtained surface is much smoother and more regular. If much larger harmonic order N is used, the particle surface obtained from the inverse SHT process becomes significantly more realistic. The reason behind is that the detailed irregularities (e.g., concavity and convexity) of the particle surface can only be captured by the harmonic coefficients at higher orders.

2.4 Morphology characterization by SH amplitudes

In section 2.2, we found that the spherical harmonic function with lower orders tend to represent the overall shape of the particle, while the spherical harmonic function with larger orders tends to represent more complex and precise morphology features. This phenomenon indicates that the harmonic coefficients at different harmonic orders have strong relationships with the

particle morphology. Thus, in this section, we aim to explore the potential relationships between particle morphology and harmonic coefficients.

The harmonic coefficients for the example particle were given in the format of the 3D histogram map, as illustrated in Fig. 3. It can be observed from the figure that the a_n^m values in each row (at each harmonic order n) are randomly distributed. Since there is no significant regular variation law of a_n^m and the uncertainty of each harmonic coefficient a_n^m is large, it is hard to identify the morphology of different particles solely from the pattern of a_n^m values. Thus, we define an amplitude parameter A_n, namely the SH amplitude at harmonic order n, to distinguish the overall contribution of the magnitude of all a_n^m at certain harmonic order n. The A_n is calculated through the following equation:

$$A_n = \sqrt{\sum_{m=-n}^{n} (a_n^m)^2} \Big/ a_0^0 \tag{10}$$

The results of A_n $(1 \leq n \leq 32)$ for the example particle in Fig. 7 (*b*) are shown in Fig. 9. It can be observed from the figure that the values of A_n show an exponential decay when n grows larger than 2. Based on the existing studies [34], in order to reconstruct the 3D particle shape, A_n can be divided into the following five categories: (1) A_0 is always equal to 1 due to the normalization of a_0^0, the value of a_0^0 determines the size of the reconstructed particle; (2) A_1 is set as 0 to ensure that the particle center is located at the origin of the coordinate system; (3) A_2 controls the elongation (ratio between the mean major principal axial length and the maximum principal axial length) and flatness (ratio between the minor major principal axial length and the mean principal axial length) of the reconstructed particle; (4) A_3 to A_{15} determine the roundness of the particle; (5) A_{16} to A_N dominate the roughness of the particle surface. The values of A_3 to A_{15} and A_{16} to A_N can be expressed by the following equations:

$$A_n = A_3\left(\frac{n}{3}\right)^{\alpha} \quad 3 \le n \le 15 \tag{11}$$

$$A_n = A_{16}\left(\frac{n}{16}\right)^{\beta} \quad 16 \le n \le N \tag{12}$$

where A_4 to A_{15} are determined by A_3 and α; A_{17} to A_N are determined by A_{16} and β. For a particular type of stones, the α and β can be obtained by linearly fitting of A_n and n under the log-log coordinates. In this study, the α and β are all set as -1.5 according to the previous studies [34].

3 Generation of 3D stone particles with desirable shapes

3.1 Random generation of 3D stones with specified A_n values

From section 2, we have two important findings: (1) the particle surface can be continuously represented by the summation of $a_n^m Y_n^m(\theta,\varphi)$, and (2) the SH amplitude A_n, namely the summation of a_n^m within each harmonic order n, has linear relationships with n under log-log coordination system, and has strong relations with the particle morphology. Thus, if the values of A_n are specified, we may reproduce the random pattern of a_n^m. Then, we are able to generate a stochastic model of particle surface through the process of inverse SHT. The process is detailed in the following steps:

(1) Given the desired value of n, A_2, A_3, A_{16}, determine the other amplitudes $A_4 \to A_{15}$ and $A_{17} \to A_n$ based on Eq. (11-12). For each amplitude A_i, there are (2i+1) number of unknown harmonic coefficients $\left[a_i^{-i},\cdots,a_i^{-m},\cdots,a_i^0,\cdots,a_i^m,\cdots,a_i^i\right]$ to be determined.

(2) Generate n series of random coefficients matrix, each matrix corresponds to a specific harmonic order i and contains (2i+1) number of random coefficient $\left[c_i^{-i},\cdots,c_i^{-m},\cdots,c_i^0,\cdots,c_i^m,\cdots,c_i^i\right]$, each coefficient c_i^m is a random variable ranging from -1 to 1.

(3) Calculate the amplitude C_i of each $\left[c_i^{-i}, \cdots, c_i^{-m}, \cdots, c_i^0, \cdots, c_i^m, \cdots, c_i^i\right]$, based on the following equation:

$$C_i = \sqrt{\sum_{m=-n}^{n} \left(c_i^m\right)^2} \tag{13}$$

(4) Determine the scaling factor k_i for each harmonic order *i* using the equation:

$$k_i = \frac{A_i}{C_i} \tag{14}$$

(5) Based on scaling factor k_i and the generated random coefficients matrix, $\left[c_i^{-i}, \cdots, c_i^{-m}, \cdots, c_i^0, \cdots, c_i^m, \cdots, c_i^i\right]$, we are able to reproduce the spherical harmonic coefficients $\left[a_i^{-i}, \cdots, a_i^{-m}, \cdots, a_i^0, \cdots, a_i^m, \cdots, a_i^i\right]$ for each harmonic order *i* based on the following equation:

$$a_i^m = k_i c_i^m \tag{15}$$

(6) Substitute all harmonic coefficients into Eq. (4) to obtain the radius function $r(\theta, \varphi)$ of the generated particle.

As can be seen from Fig. 10, by using different values of A_2, A_3 and A_{16}, we can reconstruct realistic stone particles with distinctive morphological characteristics. However, when the stone particles are reconstructed directly with A_2, A_3 and A_{16}, the shape characteristics of the stone particles can only be determined qualitatively. The accurate results of the shape index of the generated stone particles are hard to be controlled quantitatively. Therefore, it is necessary to further investigate the correlations between the harmonic amplitudes A_2, A_3 and A_{16}, and the conventional three-dimensional shape index of stone particles.

3.2 Multi-scale descriptors for quantification of stone shapes

(1) The first geometric level of particle shape – elongation and flatness

The first level particle shapes includes elongation index EI and flatness index FI. The following steps can be done to calculate EI and FI. First, the PCA algorithm is applied to process the point cloud coordinates of the particle surface to construct the OBB bounding box of the spatial point cloud. The principal components of a data set composed of point clouds can be calculated by PCA algorithm. Each point on the surface of the particle is set to $P_i(x_i, y_i, z_i)$ and then the point cloud is a data set consisting of N points P_1, P_2, …, P_N. The geometric center of the particle can be calculated as follows:

$$m(m_x, m_y, m_z) = \frac{1}{N}\sum_{i=1}^{n} P_i(x_i, y_i, z_i) \tag{16}$$

Then, the covariance matrix can be constructed:

$$C = \frac{1}{N}\sum_{i=1}^{n}(P_i - m)(P_i - m)^T \tag{17}$$

where C is consisted of six symmetric matrices as follows:

$$C_{11} = \frac{1}{N}\sum_{i=1}^{n}(x_i - m_x)(x_i - m_x)$$

$$C_{12} = C_{21} = \frac{1}{N}\sum_{i=1}^{n}(x_i - m_x)(y_i - m_y)$$

$$C_{22} = \frac{1}{N}\sum_{i=1}^{n}(y_i - m_y)(y_i - m_y) \tag{18}$$

$$C_{13} = C_{31} = \frac{1}{N}\sum_{i=1}^{n}(x_i - m_x)(z_i - m_z)$$

$$C_{33} = \frac{1}{N}\sum_{i=1}^{n}(z_i - m_z)(z_i - m_z)$$

The above covariance matrix shows the relationship among x, y, and z coordinate values. If these coordinate values are pairwise unrelated, the element value in the covariance matrix is

then 0. In order to distribute all the points uniformly along the axis, the covariance matrix needs to be converted into a diagonal matrix. Methods in linear algebra can be used:

(a) Through equation $|A - \lambda E| = 0$, the eigenvalues λ_1, λ_2, λ_3 can be solved;

(b) By plugging eigenvalues in $A - \lambda E = 0$, the corresponding eigenvectors ε_1, ε_2, ε_3 can be solved;

(c) By orthonormalizing each eigenvector, the orthogonal matrix $Q = [\varepsilon_1' \quad \varepsilon_2' \quad \varepsilon_3']$ is formed from three orthogonally normalized vectors;

Using ε_1', ε_2', ε_3' as the X, Y, and Z directions that is the natural axis of the object, the maximum and minimum positions of the particle surface point cloud along the axes X, Y, and Z can be calculated. Then, according to these maximum and minimum values, six planes of the OBB bounding box are constructed. In order to determine the maximum and minimum ranges, the inner product of the position coordinates P_i of each vertex and the unit vector is calculated. The six planes of the bounding box are:

$$\begin{aligned}
&\langle X, -\min_{1\le i\le N}\{P_i \cdot X\}\rangle \\
&\langle -X, \max_{1\le i\le N}\{P_i \cdot X\}\rangle \\
&\langle Y, -\min_{1\le i\le N}\{P_i \cdot Y\}\rangle \\
&\langle -Y, \max_{1\le i\le N}\{P_i \cdot Y\}\rangle \\
&\langle Z, -\min_{1\le i\le N}\{P_i \cdot Z\}\rangle \\
&\langle -Z, \max_{1\le i\le N}\{P_i \cdot Z\}\rangle
\end{aligned} \tag{19}$$

The size of the OBB bounding box is the difference between the maximum value and the minimum value of the corresponding inner products in X, Y, Z directions. Therefore, the difference between the maximum value and the minimum value of X, Y, Z is set to a, b and c, respectively:

$$a = \max_{1\le i\le N}\{P_i \cdot X\} - \min_{1\le i\le N}\{P_i \cdot X\} \tag{20}$$

$$b = \max_{1 \le i \le N} \{P_i \cdot Y\} - \min_{1 \le i \le N} \{P_i \cdot Y\}$$

$$c = \max_{1 \le i \le N} \{P_i \cdot Z\} - \min_{1 \le i \le N} \{P_i \cdot Z\}$$

Then the first-level shape feature – the elongation (EI) and flatness (FI) can be calculated as follows:

$$EI = \frac{b}{a}$$
$$FI = \frac{c}{b} \quad (21)$$

where the value of EI, FI changes from 0 to 1, with a trend of increasing, indicating that the particle shape changes from slender to almost equal diameter. Two groups of example stone particles with different EI and FI are illustrated in Fig. 11.

(2) The second geometric level of particle shape – roundness

Roundness is the second level shape properties that describing the corner sharpness of the 3D particle. In most of the existing study, the roundness evaluation is conducted on 2D projections of the particle, which cannot reflect the realistic condition of the 3D particle. In this study, based on the spherical harmonic function, the 3D particle roundness is calculated following the well-acknowledged Wadell's roundness definition. The calculation process is detailed in the follow steps:

Step 1: Establishment of smoothed benchmark surface

To eliminate the influence of the local surface irregularities of the 3D particles on the evaluation results of the roundness, it is necessary to smooth the outline of the particles before evaluating the roundness. Fig. 12 shows the particle surface morphology characterized by different total orders N of spherical harmonics. It can be seen that when the spherical harmonic order N is large, the reconstructed particle morphology represented by the spherical harmonic is similar to the surface morphology of the real stone. And the local unevenness is obvious when the surface of stone is irregular. When the spherical harmonic order N is low, the inverse results are obtained. Therefore, based on this characteristic, a smooth contour can be obtained by

characterizing the particle with reasonable low-order spherical harmonic parameters. This contour can be used to calculate the roundness regardless the surface roughness of the particles. Based on previous research [34], this study takes the first 16 orders spherical harmonic basis function, that is, the surface of the particle represented by N=0~15 to calculate the roundness of the particle.

Step 2: Corner area recognition based on curvature analysis of spatial surface

(a) Calculation of the largest inscribed sphere based on the 3D distance map of voxels

The recognition of the 3D corner area of the particle is determined by comparing the relative size of the local curvature radius of any point on the particle surface and the maximum inscribed sphere radius of the particle. Therefore, the maximum inscribed sphere of the particle needs to be calculated first. Using the 3D distance map algorithm, voxel gridding is performed on the space where the 3D particles are located at a certain sampling interval. Then the shortest distance from the center point of each grid to the surface of the particles is calculated as the radius of inscribed sphere centered at this point. Moreover, through iterative calculation, the grid center position with the smallest radius value is determined as the center of the inscribed sphere, then the corresponding radius is determined as the maximum inscribed sphere radius.

(b) According to the definition of the angular area in the existing literature, if the reciprocal of the local curvature (radius of curvature) of any point on the particle surface is less than the maximum inscribed sphere radius of the particle, then the point is recognized as a point on the corner area. The corner area of a particle can be considered as a partial curved surface composed of a series of adjacent corner points. Based on the existing calculation method of local curvature of the particle surface, as shown in Fig. 13 (*a*) to (*d*), four types of local curvature can be obtained, which are the maximum principal curvature K_1, the minimum principal curvature K_2, the Gaussian curvature K_{G}, and the mean curvature K_{M}.

(c) Determination of the corner area based on the comparison of the radius of curvature

According to the four types of local curvatures obtained in (b), four local curvature radii corresponding to any point on the particle surface can be calculated. Then, comparing the obtained local curvature radii with the maximum inscribed sphere of the particle obtained in

(a), all corner points belonging to corner area can be determined. Fig. 13 (*e*) ~ (*h*) shows the effect diagram of the corner area determined based on the four radii of curvature. It can be seen from the figure that the particle corner area identified by the maximum principal curvature in Fig. 13 (*e*) is the most reasonable, so the maximum principal curvature is used to determine the corner area in this study.

Step 3: Roundness calculation by sphere fitting to corner area

(a) Sphere fitting to a specified corner area

In order to evaluate the 3D roundness, it is necessary to calculate the local inscribed spheres that are fitted to the identified corner area. The main implementation steps of the algorithm are as follows:

First, calculate the inner normal vector $\vec{n}_i(\theta,\varphi)$ of the particle contour at the point $P_i(r,\theta,\varphi)$ by:

$$\vec{n}_i(\theta,\varphi)=\frac{\partial\vec{R}(\theta,\varphi)}{\partial\theta}\times\frac{\partial\vec{R}(\theta,\varphi)}{\partial\varphi} \tag{22}$$

Second, take P_i as the starting point, and take the inner normal vector $\vec{n}_i$ as the normal direction, determine an initial inscribed sphere; Third, determine whether the inscribed circle is tangent to any other point on the particle outline; Forth, If the inscribed circle is not tangent to any point on the particle contour, increasing the step length and repeat the second and third steps. If the inscribed circle is tangent to any point on the stone surface, the iteration is then terminated and the inscribed circle centered at the tangent point is taken as the local inscribed circle of the point P_i.

(b) Sphere fitting to all corners

According to the the previous section, the local inscribed circle of any corner point can be calculated. However, there are many corner points in each corner area, and the distribution characteristics of the corner area of 3D particles are different from 2D particles. For a 2D particle, the corner points of a specific corner area are connected head to end, and the corner areas are distributed independently of each other. For 3D particles, since a large number of

corner areas on the edges are connected to each other, these connected corner areas require fitting by multiple head-to-end local inscribed spheres. Therefore, it is necessary to determine the local inscribed spheres in the corner area, so that the obtained local inscribed spheres can cover all the corner areas. Moreover, a reasonable degree of overlap among local inscribed spheres is required to ensure the rationality and accuracy of the evaluation results of corner roundness. The calculation is as follows:

First, rank the corner area points from the one with largest maximum principal curvature to the one with smallest one. The larger the maximum principal curvature is, the sharper the corner is. Thus, the sphere fitting process is started with the corner point with the largest maximum principal curvature. Second, once the local inscribed sphere C_1 of the corner point with the largest maximum principal curvature is determined, eliminate the corner points that are fitted by C_1 and repeat the ranking process to determine the next local inscribed sphere C_2 that is fitted to the corner points with the largest maximum principal curvature among the rest of the corner points. Third, determining whether C_2 is overlapped with C_1. The overlapping indicator O_{ij} is defined by:

$$O_{ij} = \frac{R_i - \|C_i - C_j\|}{\|C_i - C_j\|} \tag{23}$$

where C_i represents the center position of the i_{th} local inscribed sphere that has been accepted, C_j represents the center position of the j_{th} local inscribed sphere that is to be determined, and $\|C_i - C_j\|$ represents the distance from C_i to C_j. If O_{ij} is larger than O_{thresh}, the overlap of the two local inscribed spheres is too large and C_j is not accepted. If O_{ij} is less than O_{thresh}, the overlap of the two local inscribed spheres is allowable. Forth, repeat the former two steps and determine the overlap of C_j between all the accepted local inscribed spheres. If C_j does not overlap with the exiting inscribed spheres, C_j is then accepted. Finally, iterate the former steps until the local inscribed spheres at all angular areas are involved in the overlap determination. The example results are shown in Fig. 14 (*a*). It can be seen from the figure that the number of inscribed spheres and overlap ratio generated by different O_{thresh} is significantly different. Smaller O_{thresh} indicates greater overlaps of the inscribed spheres and greater calculation cost. Furthermore, many angular areas are repeated

by different inscribed spheres. On the contrary, larger O_{thresh} indicates smaller overlaps of the inscribed spheres and smaller calculation cost. However, a too large O_{thresh} will cause certain angular areas to be ignored. Therefore, it can be seen that the inscribed spheres in the angular areas when $O_{thresh} = 0.7$ has the best fitting effect. All the angular areas are filled with spheres and the overlaps among all inscribed spheres are reasonable, so $O_{thresh} = 0.7$ is used for calculation in this study.

(c) Computation of roundness based on Waddell's definition

According to the definition of roundness by Wadell, the roundness of the particle can be calculated by combining with the maximum inscribed sphere and local inscribed spheres calculated above. The calculation formula is as follows:

$$Rd = \sum_{i=1}^{N_C} r_i \Big/ (N_C \cdot R_{insc}) \tag{24}$$

where r_i is the radius of the i_{th} inscribed corner sphere, N_C is the total number of corner spheres, R_{insc} is the radius of the maximum inscribed sphere. Two groups of example stone particles with different Rd are illustrated in Fig. 14 (*b*).

(3) The third geometric level of stone shape – roughness

The third level shape descriptor, roughness index Rg, is employed to characterize the local undulation and irregularity of the 3D stone surface. The calculation criterion of roughness is based on the definition of existing literature. Firstly, the deviation distance between the real surface and the benchmark surface is calculated. The local polyhedron formed by each triangular surface mesh element on the real stone and the corresponding element on the benchmark surface is show in Fig. xx. For the condition shown in Fig. 15 (*a*), the local deviation distance is calculated by $\Delta d_i = V_i/S_i$, which for the condition in Fig. 15 (*b*), the local deviation distance is calculated by $\Delta d_i = V_i/2S_i$, where V_i is the volume of the polyhedron, S_i is the area of the triangular surface mesh element on the real stone surface. Fig. 15 (*c*) shows the deviation distance for all the local triangular mesh element on the real stone surface. Based on the deviation distance and the weight of the local triangular mesh element on the total stone

surface, the average deviation distance based on area weighting can be calculated by:

$$\Delta\bar{d} = \frac{1}{S}\sum_{i=1}^{N_d} \Delta d_i \times S_i \tag{25}$$

Where, S_i represents the area of the i_{th} triangular mesh element, N_d represents the total number of mesh element, d_i represents the i_{th} deviation distance.

Finally, the third level stone shape descriptor - roughness index Rg is calculated by:

$$Rg = \frac{\Delta\bar{d}}{\bar{r}} \tag{26}$$

Where, $\bar{r}$ represents the average radius of the stone particle. Two groups of example stone particles with different Rg are illustrated in Fig. 15 (*d*).

3.3 Quantitative relations between A_n and shape descriptors

(1) Correlations between shape control parameters and elongation/flatness

Although the overall particle shape (first geometric level) is strongly related to A_2, the elongation and flatness of the reconstructed stones cannot be accurately controlled by using only A_2. The harmonic coefficients a_2^{-2}, a_2^{-1}, a_2^0, a_2^1, a_2^2, which are potentially able to control elongation and flatness, need to be determined. In order to determine the relationship between the harmonic coefficients and the overall shape of the particles, ellipsoids with different slenderness ratios ($EI_0 = 0.6\sim1.0$) and flatness ($FI_0 = 0.6\sim1.0$) are generated, respectively. Noted that the maximum principal axis direction of the ellipsoid particles is set to be parallel with the positive x-axis direction, the middle principal axis direction is set to be parallel with the positive y-axis direction, and the minimum principal axis direction is be parallel with the positive z-axis direction. Then, the harmonic coefficients a_2^{-2}, a_2^{-1}, a_2^0, a_2^1,

a_2^2 are obtained by using the spherical harmonic function expansion, and the results are shown in Fig. 16. It can be seen from the figure that the elongation EI_0 and flatness FI_0 are only related to a_2^0 and a_2^2. The other coefficients are very closer to 0 and can be neglected. Thus, when the elongation EI_0 and flatness FI_0 are given, we can use the following nonlinear regression equations to determine the value of a_2^0 and a_2^2:

$$a_2^0 = k_1 EI_0^3 + k_2 EI_0^2 FI_0 + k_3 EI_0 FI_0^2 + k_4 FI_0^3 + k_5 EI_0^2 + k_6 EI_0 FI_0 + k_7 FI_0^2 + k_8 EI_0 + k_9 FI_0 + k_{10} \quad (27)$$

$$a_2^2 = k_1 EI_0^3 + k_2 EI_0^2 FI_0 + k_3 EI_0 FI_0^2 + k_4 FI_0^3 + k_5 EI_0^2 + k_6 EI_0 FI_0 + k_7 FI_0^2 + k_8 EI_0 + k_9 FI_0 + k_{10} \quad (28)$$

where the coefficients k_i are summarized in Table 1.

To ensure that the reconstructed virtual stone particles satisfied the target elongation and flatness, 1000 virtual particles with various $EI_0 \in [0.6, 1.0]$, $FI_0 \in [0.6, 1.0]$, $A_3 \in [0.0, 0.1]$ and $A_{16} \in [0.0, 0.016]$ are generated. The elongation and flatness are subsequently calculated for all generated particles. The results of the generated elongation EI^{gen} are plotted against EI_0, FI_0, A_3 and A_{16} in Fig. 17. It can be inferred from the above figure that EI_0 is strongly correlated with EI^{gen} while FI_0, A_3 and A_{16} have no influence on EI^{gen}. This result indicates that we are able to effectively and conveniently control the elongation of the generated stones through the adjustment of only one parameter EI_0. When the desired value of EI^{gen} is given, we can use the following regression equation to determine the control parameter EI_0 for particle generation:

$$EI_0 = 1.0636 EI^{gen} - 0.0731 \quad (29)$$

In addition, the results of the generated flatness FI^{gen} are plotted against EI_0, FI_0, A_3 and A_{16} in Fig. 18. It can be inferred from the above figure that FI_0 is strongly correlated with FI^{gen} while EI_0, A_3 and A_{16} have no influence on FI^{gen}. This result indicates that we are able to effectively and conveniently control the flatness the generated stones through the adjustment of only one parameter FI_0. When the desired value of FI^{gen} is given, we can use the following regression equation to determine the control parameter FI_0 for particle generation:

$$FI_0 = 1.0407FI^{gen} - 0.0552 \tag{30}$$

(2) Correlations between shape control parameters and roundness

It can be seen from Fig. 10 (*b*) that A_3 is relevant to the second geometric level of particle shape Rd. To ensure that the reconstructed virtual stone particles satisfied the target roundness, another 1000 virtual particles with various $EI_0 \in [0.6, 1.0]$, $FI_0 \in [0.6, 1.0]$, $A_3 \in [0.0, 0.1]$ and $A_{16} \in [0.0, 0.016]$ are generated. The roundness is subsequently calculated for all generated particles. The results of the generated Rd^{gen} are plotted against EI_0, FI_0, A_3 and A_{16} in Fig. 19. It can be inferred from the figure that A_3 is strongly correlated with Rd^{gen} while EI_0, FI_0 and A_{16} have no influence on Rd^{gen}. The result indicates that the roundness of the generated stones can be effectively and conveniently controlled through the adjustment of only one parameter A_3. When the desired value of Rd^{gen} is given, the following regression equation can be used to determine the control parameter A_3 for particle generation:

$$A_3 = -0.39Rd^{gen3} + 1.01Rd^{gen2} - 0.91Rd^{gen} + 0.28 \tag{31}$$

(3) Correlations between shape control parameters and roughness

It can be seen from Fig. 10 (*c*) that A_{16} is relevant to the third geometric level of particle shape – roughness. To ensure that the reconstructed virtual stone particles satisfied the target roughness, another 1000 virtual particles with various $EI_0 \in [0.6, 1.0]$, $FI_0 \in [0.6, 1.0]$, $A_3 \in [0.0, 0.1]$ and $A_{16} \in [0.0, 0.016]$ are generated. The roughness is subsequently calculated for all generated particles. The results of the generated Rg^{gen} are plotted against EI_0, FI_0, A_3 and A_{16} in Fig. 20. It can be inferred from the figure that A_{16} is strongly correlated with Rg^{gen} while EI_0, FI_0 and A_3 have no influence on Rg^{gen}. The result indicates that we can effectively and conveniently control the roundness of the generated stones through the adjustment of only one parameter A_{16}. When the desired value of Rg^{gen} is given, we can use the following regression equation to determine the control parameter A_{16} for particle generation:

$$A_{16} = 12.028Rg^{gen^2} - 0.6716Rg^{gen} \tag{32}$$

In order to verify the validity of the above four regression Eqs. (29-32), a particle generation example is illustrated as follows. First, the desired values of the target shape are given $EI^{tar} = 0.6$, $Rd^{tar} = 0.9$ and $Rg^{tar} = 0.01$. Then, according to the regression formula, the corresponding shape control parameters EI_0, A_3 and A_{16} are inversely calculated. According to the determined shape control parameters, 1000 virtual stone particles are randomly generated, and the shape indexes of particles (EI^{gen}, Rd^{gen} and Rg^{gen}) are calculated. Finally, we compare the shape target values of 1000 "test" particles with the statistical results of reconstructed shapes. As shown in Fig. 21, the peak value of the shape

index probability density distribution curve of the reconstructed particle is very close to its target value, which shows that based on the regression equation proposed in this paper, the reconstructed particle shape can be very close to the target value in a large probability. It can be observed from the probability distribution curve that: (1) the distribution of EI^{gen} is widest, and the peak value shifts to the left of EI^{tar}; (2) the distribution of Rd^{gen} is slightly wider, and the peak value shifts to the right of Rd^{tar}; (3) The distribution of roughness Rg^{gen} is the thinnest and the peak value is approximately in the middle, which is very close to Rg^{tar}.

3.4 Control of generated stone morphology by IMC approach

It can be seen from the previous section that although the target shapes of the "test" particles are linearly related to the shapes of the reconstructed ones, the statistical results still show obvious discreteness. This indicates that there are certain errors between the reconstructed shapes and the target shapes. In order to reduce the errors, the inverse Monte Carlo method is employed to adjust the reconstructed particle shape.

Firstly, the average relative error e_{ave}^{*} is defined as the index to quantify the matching degree between the reconstructed shape and the target shape, and the upper corner sign * represents the abbreviation of the specific shape index. Taking the elongation EI as an example, the calculation formula of the average relative error e_{ave}^{EI} is as follows:

$$e_{ave}^{EI} = \frac{1}{N_P}\sum_{i=1}^{N_P} e_i^{EI} \tag{33}$$

$$e_i^{EI} = \frac{\left|EI_i^{gen} - EI_i^{tar}\right|}{EI_i^{tar}} \tag{34}$$

where e_i^{EI} represents the relative error of the elongation of the i^{th} reconstructed particle, EI_i^{gen} represents the elongation of the i^{th} reconstructed particle, EI_i^{tar} represents the target value of the slenderness of the i^{th} particle, and N_P represents the total number of particles.

Based on the average relative error e_{ave}^{EI}, the following steps are used to adjust the particle shape results so that the error between the reconstructed shape and the target shape can be gradually reduced:

Step (1): Determine the target 3D shape parameters, EI^{tar}, FI^{tar}, Rd^{tar}, and Rg^{tar}. Substitute the target shape parameters into the four regression equations to determine the shape control parameters, EI_0, FI_0, A_3, and A_{16}.

Step (2): Substitute EI_0 and FI_0 into Eq. (29-30) to acquire the harmonic coefficients a_2^0 and a_2^2. Substitute A_3 and A_{16} into Eq. (11-12) to acquire A_4 to A_{15} and A_{17} to A_n. Then, the harmonic coefficients a_i^m $(3 \leq i \leq n)$ can be determined following the procedure as mentioned in section 3.1. Substitute all acquired harmonic coefficients into Eq. (4) to obtain the coordinates $r(\theta, \varphi)$ of the surface points in the spherical coordinate system.

Step (3): Perform 3D particle shape analysis on the reconstructed particles to acquire a series of elongation, flatness, roundness and roughness parameters (EI^{gen}, FI^{gen}, Rd^{gen} and Rg^{gen}). Based on Eq. (34), calculate the relative error for each shape parameter of each particle, e_i^{EI}, e_i^{FI}, e_i^{Rd} and e_i^{Rg}. Based on Eq. (33), calculate the average relative error for each shape

parameter, e_{ave}^{EI}, e_{ave}^{FI}, e_{ave}^{Rd} and e_{ave}^{Rg}. If e_{ave}^{EI}, e_{ave}^{FI}, e_{ave}^{Rd} and e_{ave}^{Rg} are larger than the target threshold, e^{tar}, delete the particles with e_i^{EI}, e_i^{FI}, e_i^{Rd} or e_i^{Rg} larger than e^{tar}. Regenerate the deleted particle following step (2).

Step (4): Repeat step (3) until all particles have e_{ave}^{EI}, e_{ave}^{FI}, e_{ave}^{Rd} and e_{ave}^{Rg} smaller than e^{tar}.

In order to verify the effectiveness of the proposed inverse Monte Carlo algorithm for the precise control of the reconstructed three-dimensional particle shape, a set of target shape parameters EI^{tar}, FI^{tar}, Rd^{tar} and Rg^{tar} are prescribed. Based on the equations given in section 3.3, calculate the corresponding harmonic parameters a_2^0, a_2^2, A_3 and A_{16}. Use the proposed algorithm to reconstruct a set of "test" particles. Calculate the shape parameters, EI^{gen}, FI^{gen}, Rd^{gen} and Rg^{gen}, of the "test" stones. Compare the EI^{tar}, FI^{tar}, Rd^{tar} and Rg^{tar} versus EI^{gen}, FI^{gen}, Rd^{gen} and Rg^{gen} in Fig. 22. It can be seen from the figure that the EI^{gen}, FI^{gen}, Rd^{gen} and Rg^{gen} are approximately identical to EI^{tar}, FI^{tar}, Rd^{tar} and Rg^{tar}. Among them, EI^{gen}, FI^{gen}, Rd^{gen} have relatively poor correlations withEI^{tar}, FI^{tar}, Rd^{tar}, while Rg^{gen} has the best correlation with Rg^{tar}. Then, the particle shapes of the generated particles are precisely controlled by the inverse Monte Carlo algorithm, e^{tar} is set to 0.01. The results are shown in Fig. 23. It can be seen from the figure that after the precise control of particle shape based on the inverse Monte Carlo algorithm, the correlation of each shape parameter increases significantly.

4 Allocation of stone particles with controlled geometries

4.1 Stone particle collision detection

In most of the stone-based materials, the stone inclusions are non-overlapping stone particles, which are randomly distributed inside the material. Thus, the generated stone particles are required to be distributed into the specimen area individually. During particles allocation, collision detection is required to determine the acceptance of the assigned particle locations. To make the allocation process less computationally intensive, the collision detection between the allocated particle and the existing particles is divided into two steps: rapid broad-phase collision detection and efficient narrow-phase collision detection.

(1) Rapid broad-phase collision detection

In the first step, both the allocated and existing stone particles are circumscribed by the axis-aligned bounding boxes (AABBs). The boundaries $(X_{min}, X_{max}, Y_{min}, Y_{max}, Z_{min}, Z_{max})$ of AABB for a particular particle is illustrated in Fig. 24 (*a*). Then, the sample domain is divided into $N_{bx} \times N_{by} \times N_{bz}$ cubic bins, and the obtained AABBs are entered into cells (i.e., spatial bins) in the cell space based on an enlarged extent (i.e., cell extent). Once the cell extents of two stone particles overlap, the pair of two stone particles is considered as a collision candidate as shown in Fig. 24 (*b*) and (*c*). More specifically, if an allocated particle shares at least one single cell bin with the existing one, further detection is required to examine the potential collision.

(2) narrow-phase collision detection

In the second step, a node-to-surface algorithm is developed to identify the accurate collision condition of two collision candidates. Assume particle A is the one to be allocated, and particle B is one of the existing particles which are identified as the potentially overlapped with A. First, discretize particle A into m number of surface points $\left[P_1^A, \cdots, P_i^A, \cdots, P_m^A\right]$. Then, transform the global coordinate $\left(x_i^A, y_i^A, z_i^A\right)$ of each surface point P_i^A into the spherical coordinate $\left(R_i'^A, \theta_i'^A, \varphi_i'^A\right)$ at the local spherical coordination of particle B.

Next, the continuous closed surface of particle B is represented by the spherical harmonic function:

$$r^B(\theta, \varphi) = AF_B \sum_{n=0}^{N} \sum_{m=-n}^{n} a_{B_n}^{\ m} Y_n^m(\theta, \varphi) \tag{35}$$

For each surface point P_i^A of particle A, a relative distance Γ_i can be calculated to identify the spatial position of P_i^A with regard to particle B:

$$\Gamma_i = R_i'^A - r^B\left(\theta_i'^A, \varphi_i'^A\right) \tag{36}$$

If Γ_i is positive, $R_i'^A$ is larger than $r^B\left(\theta_i'^A, \varphi_i'^A\right)$, which means surface point P_i^A is outside particle B. If Γ_i is negative, P_i^A is identified to be inside particle B. Repeat the calculation of Γ_i for each surface point of particle A, once a point P_i^A is identified to have a negative Γ_i, the iteration can be terminated and particle A is then determined as collision with particle B, which indicates that the allocation is failed, as illustrated in Fig. 24 (*d*). Only when all Γ_i of particle A is positive, the allocation of particle A is succeeded, and the position of particle A is then settled.

4.2 Procedure of numerical model generation

In this study, the model generation for stone-based material with quantitative controlled stone inclusion features is coded in MATLAB. The procedure to implement the program is detailed as following steps:

(1) Specify sample domain

In this study, the sample domain is a rectangular shape, and the domain dimension is given as length= L_0, width= W_0, and height= H_0. The sample domain volume can be obtained as $V_{sample} = L_0 \times W_0 \times H_0$.

(2) Specify stone content and stone sizes

Given the desired stone content, W_{stone}, the total volume of the stone inclusion can be calculated as $V_{stone} = V_{sample} \times W_{stone}$. Given the volumetric gradation curve $G(\boldsymbol{V})$ of the desired stone particles, the probability distribution function of $G(\boldsymbol{V})$ is given by $g(\boldsymbol{V}) = dG(\boldsymbol{V})/d\boldsymbol{V}$. Then, the number of the stone particles, N_{stone}, can be obtained [2]:

$$N_{stone} = V_{stone} \int_{V_{min}}^{V_{max}} \frac{\mathrm{g}(\boldsymbol{V})}{\boldsymbol{V}} d\boldsymbol{V} \tag{37}$$

where V_{min} and V_{max} are the minimum and maximum values of the allocated stone volume.

In addition, the number-percentage-based cumulative density function $F(\boldsymbol{V})$ of the volumetric stone sizes can be obtained by [2]:

$$F(\boldsymbol{V}) = \frac{\mathrm{V_{stone}}}{\mathrm{N_{stone}}} \int_{V_{min}}^{\boldsymbol{V}} \frac{\mathrm{g}(\boldsymbol{V})}{\boldsymbol{V}} d\boldsymbol{V} \tag{38}$$

Next, the volume v_i of each stone can be calculated based on the inverse transform sampling (ITS) method [2]:

$$v_i = F^{-1}(U_i) \tag{39}$$

where $F^{-1}(x)$ is the inverse function of $F(x)$. U_i is one of the generated random numbers $(U_1, U_2, U_3 \ldots, U_{N_{stone}})$ which are uniformly distributed from 0.0 to 1.0.

(3) Generate stone models of desired shapes

Given the desired stone shapes, EI^{tar}, FI^{tar}, Rd^{tar} and Rg^{tar}, generate the corresponding stone particle models. Each generated stone particle SP_i is represented in the form of spherical harmonic function:

$$r_i(\theta, \varphi) = AF_i \sum_{n=0}^{N} \sum_{m=-n}^{n} a_{i_n}^{m} Y_n^m(\theta, \varphi) \tag{40}$$

where the harmonic coefficients $a_{i_n}^{m}$ are determined by the desired stone shapes EI_i^{tar}, FI_i^{tar}, Rd_i^{tar}, and Rg_i^{tar}; AF_i is the amplification factor to determine the volume of the stone particle:

$$AF_i = v_i \Big/ \left[\int_0^{\pi} \int_0^{2\pi} \sum_{n=0}^{N} \sum_{m=-n}^{n} a_{i_n}^{m} Y_n^m(\theta, \varphi)\, d\theta\, d\varphi \right] \tag{41}$$

(4) Allocate stone particles into sample domain

Rank the particles from the largest one to the smallest one. For each stone particle, SP_i, the geometric center is determined by:

$$\begin{cases} x_c = L_0 \times \varepsilon_1 \\ y_c = W_0 \times \varepsilon_2 \\ z_c = H_0 \times \varepsilon_3 \end{cases} \tag{42}$$

where ε_1, ε_2, and ε_3 are randomly selected discrete variables ranging from 0.0 to 1.0. Since the stone particle center (x_c, y_c, z_c) is randomly determined, an allocated stone particle might overlap with the existing stone or exceed the domain boundary. Employ the collision detection algorithm to justify the acceptability of the allocated particle. Repeat the process until all stone particles are successively allocated into the sample domain. The workflow of the procedure is shown in Fig. 25.

4.3 Example models of the stone-based material

Using the above-detailed algorithms, we are able to generate various numerical models of stone-based materials with quantitatively controlled stone inclusion features. First, in order to further illustrate the capability of the three-dimensional particle reconstruction algorithm proposed in this study, two sets of particle reconstruction examples are carried out. The first group aims to generate pebble-like particles with different elongation and flatness. When reconstructing particles, the target values of elongation and flatness are set to 0.7, 0.8, 0.9 and 1.0 respectively, while the roundness and roughness remain unchanged. The second group is equant-shape particles with different roundness and roughness. When reconstructing the particles, the fine length and flatness are both taken as 1.0, while the changes of edge roundness and roughness are taken as 0.30, 0.45, 0.60, 0.75 and 0.000, 0.004, 0.008 and 0.012, respectively. The reconstructed three-dimensional particle model is shown in Fig. 26. Next, to illustrate the capability of the proposed approach, three groups of numerical examples are reproduced with

(1) various stone contents, (2) with various stone size distributions, and (3) with various stone shapes, as shown in Fig. 27. It worth noted that the random stone allocation algorithm has a limitation on stone content. When the target stone content is higher than 50%, further simulations, e.g., isotropic compression in DEM, is required to densify the assembly.

5 Applications to DEM simulation of stone-based materials

5.1 Preparation of numerical samples

In this section, the proposed algorithm is applied to modeling the triaxial compression tests of stone-based material. Four groups of stone-based materials are simulated with distinctive stone inclusion features. Group A aims to simulate the stone-soil mixtures with irregular stone particles of five different stone contents, i.e., B_C=15%, 30%, 45%, 60%, and 75%. Group B aims to simulate stone-based materials of 90% stone content with five different stone elongation, i.e., EI=1.0, 0.9, 0.8, 0.7, 0.6. Group C aims to simulate stone-based materials of 90% stone content with five different stone flatness, i.e., FI=1.0, 0.9, 0.8, 0.7, 0.6. Group D aims to simulate stone-based material of 90% stone content with five different stone roundness, i.e., Rd=1.0, 0.9, 0.8, 0.7, 0.6. In each group, numerical samples are prepared with the same stone size, d_{stone}=100mm.

After the initial samples are produced based on the proposed algorithms as detailed in the previous sections, the triangular mesh models in the format of "STL" files are imported into the well-acknowledged DEM software PFC3D and the bubble packing algorithm is subsequently employed to transform the generated stone model into the clump-particle model. Then, fine spheres of mean diameter, $d_{fine} = d_{stone}/4$, are generated to fill the void space, which

simulates the soil matrix. Based on the previous studies [39], the modeling parameters of stone-based material used in the DEM simulations are summarized as: (a) the particle density is 2600kg/m^3; (b) friction between rigid particles during shearing process is 0.5; (c) friction between wall and rigid particles is 0.0; (d) contact modulus between wall and rigid particles is 1×10^9; (e) contact modulus between rigid particles is 1×10^8; (f) the ratio between normal and shear stiffness is 4/3; (g) damping ratio is 0.7.

5.2 Process of triaxial compression test

The realistic large-scale triaxial compression test is simulated by imposing axial loading from vertical direction by two rigid walls and maintain confining pressure from horizontal direction by membrane-based servo control process, as detailed in the authors' previous work [40]. The major procedure is summarized as follow: (1) According to the sample preparation process in the laboratory, rock stones and fine particles are generated and compacted layer by layer a cylindrical steel container simulated by rigid walls in DEM; (2) Delete the cylindrical sidewalls and generate the bonded cluster-based particle along the sidewalls to simulate the membrane; (3) Activate the lateral confining pressure of 200 kPa based on the membrane servo method and the axial confining pressure of 200kPa based on the wall servo method. The example models of the preshear sample with different stone contents are illustrated in Fig. 28 (*a*) ~ (*c*); (4) The wall at the top is moved downward to activate the axial loading to the specimen at a constant strain rate. Meanwhile, the membrane servo process is maintained to ensure that the confining pressure are always equal to the desired value (200 kPa in this study) [40]. The shear

strain rate is set to low enough to ensure that the model is at the quasi-static state. The shearing process is stopped when the shear strain approaches 30%. The samples with different stone contents at the final state are illustrated in Fig. 28 (*d*) ~ (*f*).

5.3 Macro- and micromechanical response

(1) Shear strength and deformation

The deviator stress ratio η is computed to reflect the evolution of mechanical strength of the stone-based materials during shearing, which is defined as:

$$\eta = \frac{q}{p'} \tag{43}$$

where q is the deviatoric stress and p is the mean effective stress, which can be calculated by the stress tensors:

$$q = \sqrt{3J_2} \tag{44}$$

$$p' = \frac{1}{3}I_1 \tag{45}$$

where J_2 is the second order invariant of the deviator stress tensor σ'_{ij}; I_1 is the first order invariant of the stress tensor σ_{ij}. They can be calculated by:

$$J_2 = \sigma'_{ij}\sigma'_{ij}/2 \tag{46}$$

$$I_1 = \sigma_{ii} \tag{47}$$

where the stress tensor σ_{ij} is computed by:

$$\sigma_{ij} = \frac{1}{V}\sum_{c\in V} f_i^c l_j^c \tag{48}$$

where the l^c is the branch vector, f^c is the contact force, and V is the volume of the assembly.

The axial strain ε_1 and volumetric strain ε_v of the triaxial shear sample can be calculated as follow:

$$\varepsilon_1 = -\int_{H_0}^{H} \frac{dh}{h} = \ln\frac{H_0}{H} \tag{49}$$

where H is the current sample height; H_0 is the initial sample height. The calculation of ε_v is detailed in the authors' previous work [40]. The positive value of ε_v indicate a contraction state while a negative value of ε_v indicate a shear dilation state of the sample.

Fig. 29 illustrates the results of the deviator stress ratio η for the four groups of stone-based materials. For all the simulated specimen, the η-ε_1 curves behave in a similar fashion, showing peak stress, i.e., the stress softening. AR tends to have a greater influence on post peak behaviors. For specimens with different stone contents, both the peak and residual values of η are positively related to B_C and exhibit significant increment when B_C increase from 60% to 75%. For specimens with different form-scale shapes, the specimen show more significant decreasing in both peak and residual values of η when EI and FI increase from 0.6 to 1.0. For specimens with different roundness, the peak η exhibit more significant increment than the residual η when Rd decrease from 0.9 to 0.5. Fig. 30 illustrates the results of the volumetric changes for the four groups of stone-based materials during shearing. It can be seen

from the figure that the lower stone content B_C tends to reduce the dilatancy, while lower values of EI, FI and Rd tend to increase the volumetric deformation.

(2) Mean coordination number

As shown in Fig. 31, the mean coordination number Z reveals the evolution of the internal packing structure of the stone-based materials during shear. In all cases, Z exhibits an exponential drop versus the increasing axial strain during the initial shearing process. For group B and group C, the values of Z are always positively related to EI and FI during the whole shear process, i.e., Z increases from 6 to 8 at the initial state and shifts from 4.0 to 4.7 at the residual state when the EI and FI varies from 0.6 to 1.0. For group D, Z only shows more significantly positive relations with Rd during the residual shear process. At the residual state, Z decreases from 4.2 to 3.7 when Rd decreases from 0.9 to 0.5.

(3) Percentage of sliding contact

The sliding contacts are governed by Coulomb's friction law. The sliding ratio R_{sc} is denoted as the ratio between shear force f_t and normal force f_n at each contact:

$$R_{sc} = |f_t|/(\mu_c f_n) \tag{50}$$

We assumed that sliding event occurs at contact when $R_{sc} > 0.99$. Then, the percentage of sliding contact P_{sc} can be defined as:

$$P_{sc} = \sum_{i=1}^{N_c} G(R_{sc}) \Big/ N_c$$
$$G(R_{sc}) = \begin{cases} 0 & R_{sc} \leq 0.99 \\ 1 & R_{sc} > 0.99 \end{cases} \tag{51}$$

where N_c is the total number of contacts.

Fig. 32 displays the evolution of P_{sc} versus axial strain ε_a. In general, the four groups of numerical specimens show similar trends of P_{sc}-ε_1 curves, in which P_{sc} increases sharply to a peak value, and then gradually decreases to a steady-state. For group A, P_{sc} increases from 25% to 35% at the peak state, and increases from 18% to 24% at the steady-state, when stone content W_C increases from 15% to 75%. The specimen with larger stone content shows a more significant increment of P_{sc}. For group B and C, the samples show negative relationships between peak P_{sc} and the form particle shapes, i.e., the peak value of P_{sc} increases from 38% to 56% and the residual value of P_{sc} increases from 31% to 40% when EI and FI decreases from 1.0 to 0.6. For group D, compared with W_C, EI and FI, Rd shows less influence on P_{sc}.

6 Conclusions

In this paper, realistic stone particle morphologies are reconstructed via the inverse operation of spherical harmonic transformation. Then, quantitative control of the stone-inclusion features, including the particle shape, stone size distribution, stone content is implemented via several proposed algorithms. The capability of the proposed approach is validated using several examples, in which samples with different stone contents, stone size distributions, and stone shape features are generated in a quantitative and precise manner. The key innovations of the proposed study are summarized as follow:

(1) Four shape control parameters (EI_o, FI_o, A_3, A_{16}) are proposed to generate realistic stone particles with prescribed shape features through the inverse operation of spherical harmonic transformation.

(2) The nonlinear regression analysis of the traditional shape descriptors (EI, FI, Rd, and Rg) and Fourier amplitude parameters (EI_o, FI_o, A_3, A_{16}) are performed to determine the average shape features of the generated stone particles. The deviations between the generated shape results and the target values are adjusted based on the Inverse Monte-Carlo approach.

(3) The global and local overlapping detection algorithms are developed to allocate stone particles to the sample domain rapidly by considering realistic stone-inclusion features of stone-based materials, including their stone contents, stone size distributions, and stone orientations.

Using the developed approach, four groups of triaxial compression tests were conducted on stone-based materials with different stone contents and stone shapes to illustrate its feasibility and capability. The simulation results demonstrate that the developed approach is useful to investigate the effects of stone inclusion features on the macro- and micro-mechanical behaviors of realistic stone-based materials.

References

[1] Dai, Q. Two- and three-dimensional micromechanical viscoelastic finite element modeling of stone-based materials with x-ray computed tomography images. Construction & Building Materials, (2011). 25(2), 1102-1114.

[2] Wang, X., Liang, Z., Nie, Z., & Gong, J. Stochastic numerical model of stone-based

materials with realistic stone-inclusion features. Construction and Building Materials, (2019). 197(10), 830-848.

[3] Liu, Y., You, Z., Li, L., & Wang, W. Review on advances in modeling and simulation of stone-based paving materials. Construction & Building Materials, (2013). 43, 408-417.

[4] Neal, A., Pontee, N. I., Pye, K., & Richards, J. (2010). Internal structure of mixed-sand-and-gravel beach deposits revealed using ground-penetrating radar. Sedimentology, 49(4).

[5] Zhang, P., Gao, Z., Shi, Y., Lin, Y., & Li, J. Effect of large broken stone content on properties of roller compacted concrete based on fractal theory. Construction and Building Materials, (2020). 262, 120821.

[6] Rodrigues, E. A., Gimenes, M., Luís A.G. Bitencourt Jr, & Manzoli, O. L. A concurrent multiscale approach for modeling recycled aggregate concrete. Construction and Building Materials. (2020).

[7] Wang, Y., Li, C. H., & Hu, Y. Z. Use of x-ray computed tomography to investigate the effect of rock blocks on meso-structural changes in soil-rock mixture under triaxial deformation. Construction & Building Materials, (2018). 164, 386-399.

[8] Matsumoto, H. , & Young, A. . (2018). Automated cobble mapping of a mixed sand-cobble beach using a mobile lidar system. Remote Sensing, 10(8).

[9] Hashemi, S. . (2002). The design of a relational database on the geotechnical properties of northern england glacial till. Newcastle University.

[10] Koohmishi, M., & Palassi, M. Effect of gradation of aggregate and size of fouling materials on hydraulic conductivity of sand-fouled railway ballast. Construction and Building Materials, (2018). 167, 514-523.

[11] Chen, J., Gao, R., Liu, Y., Shi, Z., & Zhang, R. Numerical exploration of the behavior of coal-fouled ballast subjected to direct shear test. Construction and Building Materials, (2021). 273, 121927.

[12] De Bold, R., Connolly, D. P., Patience, S., Lim, M., & Forde, M. C. Using impulse response testing to examine ballast fouling of a railway trackbed. Construction and Building Materials, (2021). 274, 121888.

[13] Yang, H., Rao, M., & Dong, Y. Influence study of extra-large stone limited size and

content on full-graded concrete properties. Construction and Building Materials, (2016). 127, 774-783.

[14] Elmouttie, M. K., & Poropat, G. V. A method to estimate in situ block size distribution. Rock Mechanics & Rock Engineering, (2012). 45(3), 401-407.

[15] Kumara, J.J., & Hayano, K. Importance of particle shape on stress-strain behaviour of crushed stone-sand mixtures. Geomechanics and Engineering, (2016). 10(4), 455-470.

[16] Khorasani, E. , Amini, M. , Hossaini, M. F. , & Medley, E. Evaluating the effects of the inclinations of rock blocks on the stability of bimrock slopes. Geomechanics and Engineering, (2019). 17(3), 281-287.

[17] Napoli, M. L., Barbero, M., Ravera, E., & Scavia, C. A stochastic approach to slope stability analysis in bimrocks. International Journal of Rock Mechanics and Mining Sciences, (2018). 101, 41-49.

[18] Napoli, M. L. , Barbero, M. , Ravera, E. , & Scavia, C. A stochastic approach to slope stability analysis in bimrocks. International Journal of Rock Mechanics and Mining Sciences, (2018). 101, 41-49.

[19] Afifipour, M., & Moarefvand, P. Experimental study of post-peak behavior of bimrocks with high rock block proportions. Journal of Central South University, (2014a). 21(2), 761-767.

[20] Afifipour, M., & Moarefvand, P. Mechanical behavior of bimrocks having high rock block proportion. International Journal of Rock Mechanics and Mining Sciences, (2014b). 65, 40-48.

[21] Zhang, H. Y., Xu, W. J., & Yu, Y. Z. Numerical analysis of soil-rock mixture's meso-mechanics based on biaxial test. Journal of Central South University, (2016). 23(3), 685-700.

[22] Coli, N., Berry, P., & Boldini, D. In situ non-conventional shear tests for the mechanical characterisation of a bimrock. International Journal of Rock Mechanics and Mining Sciences, (2011). 48(1), 95-102.

[23] Mahdevari, S., & Maarefvand, P. Applying ultrasonic waves to evaluate the volumetric block proportion of bimrocks. Arabian Journal of Geosciences, (2017). 10(9), 204.

[24] Wang, Y., Li, X., Hu, R. L., Li, S. D., & Wang, J. Y. (2015). Experimental study of the ultrasonic and mechanical properties of SRM under compressive loading. Environmental Earth Sciences, 74(6), 5023-5037.

[25] Afifipour, M., & Moarefvand, P. (2014). Mechanical behavior of bimrocks having high rock block proportion. International Journal of Rock Mechanics and Mining Sciences, 65, 40-48.

[26] Zhang, S., Tang, H., Zhan, H., Lei, G., & Cheng, H. Investigation of scale effect of numerical unconfined compression strengths of virtual colluvial–deluvial soil–rock mixture. International Journal of Rock Mechanics and Mining Sciences, (2015). 77, 208-219.

[27] Coli, N., Berry, P., Boldini, D., & Bruno, R. The contribution of geostatistics to the characterisation of some bimrock properties. Engineering geology, (2012). 137, 53-63.

[28] Khorasani, E., Amini, M., Hossaini, M. F., & Medley, E. Statistical analysis of bimslope stability using physical and numerical models. Engineering Geology, (2019). 254, 13-24.

[29] Meng, Q. X., Wang, H. L., Xu, W. Y., & Cai, M. A numerical homogenization study of the elastic property of a soil-rock mixture using random mesostructure generation. Computers and Geotechnics, (2018). 98, 48-57.

[30] Xu, W. J., Wang, S., Zhang, H. Y., & Zhang, Z. L. Discrete element modelling of a soil-rock mixture used in an embankment dam. International Journal of Rock Mechanics and Mining Sciences, (2016). 86, 141-156.

[31] Xu, W. J., Zhang, H. Y., Jie, Y. X., & Yu, Y. Z. Generation of 3D random meso-structure of soil-rock mixture and its meso-structural mechanics based on numerical tests. Journal of Central South University, (2015). 22(2), 619-630.

[32] Chen, L., Yang, Y., & Zheng, H. Numerical study of soil-rock mixture: Generation of random aggregate structure. Science China Technological Sciences, (2018). 61(3), 359-369.

[33] Schmit, J., & Olszak, A. High-precision shape measurement by white-light interferometry with real-time scanner error correction. Applied Optics, (2002). 41(28), 5943-50.

[34] Deheng, W., Jianfeng, W., Jiayan, N., & Bo, Z. Generation of realistic sand particles with

fractal nature using an improved spherical harmonic analysis. Computers and Geotechnics, (2018). 104, 1-12.

[35] Wadell, & Hakon. Sphericity and roundness of rock particles. Journal of Geology, (1933). 41(3), 310-331.

[36] Zhihong, N. , Zhengyu, L. , Xiang, W. , & Jian, G. . Evaluation of granular particle roundness using digital image processing and computational geometry. Construction and Building Materials, (2018). 172, 319-329.

[37] Nie, Z., Liang, Z., & Wang, X. A three-dimensional particle roundness evaluation method. Granular Matter, (2018). 20(2), 32.

[38] Wang, X. Shape quantification, model reconstruction of geotechnical granular materials and application to discrete element modeling, Central South University, Changsha, Hunan, China. (2020). Doctoral dissertation.

[39] Gong Jian. Meso mechanical properties of soil rock mixture, Dalian University of Technology, Dalian, Shandong, China (2017). Doctoral dissertation.

[40] Zhang, J., Wang, X., Yin, Z. Y., & Liang, Z. Dem modeling of large-scale triaxial test of rock clasts considering realistic particle shapes and flexible membrane boundary. Engineering Geology, (2020). 279, 105871.

Table

Table 1 The coefficients of the regression function for a_2^0 and a_2^2

coefficients	a_2^0	a_2^2
k_1	0.3831	-0.8004
k_2	0.4299	-0.3769
k_3	0.4569	-0.3523
k_4	0.6548	-0.1237
k_5	-1.5492	2.8077
k_6	-1.6886	1.3563
k_7	-2.4093	0.6781
k_8	2.4920	-3.8596
k_9	3.5251	-1.2751
k_{10}	-2.2935	1.9448

Figures

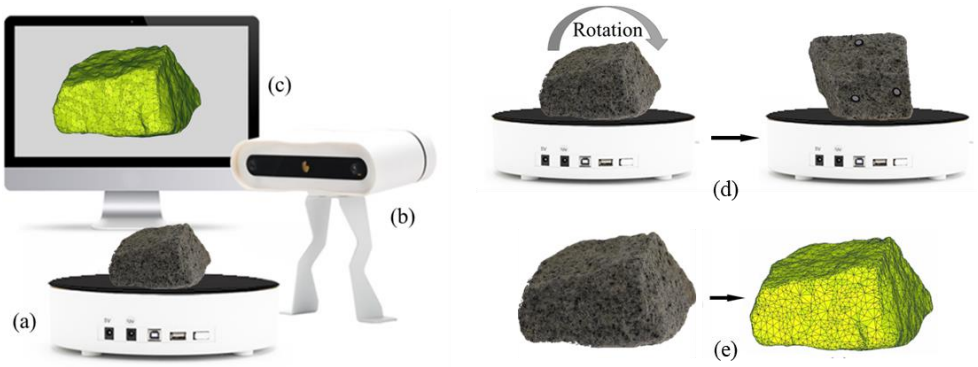

Fig. 1 Schematic diagram of white light scanner: (a) turntable; (b) image acquisition device; (c) computer; (d) rotation of the scanning target; (e) triangular mesh model

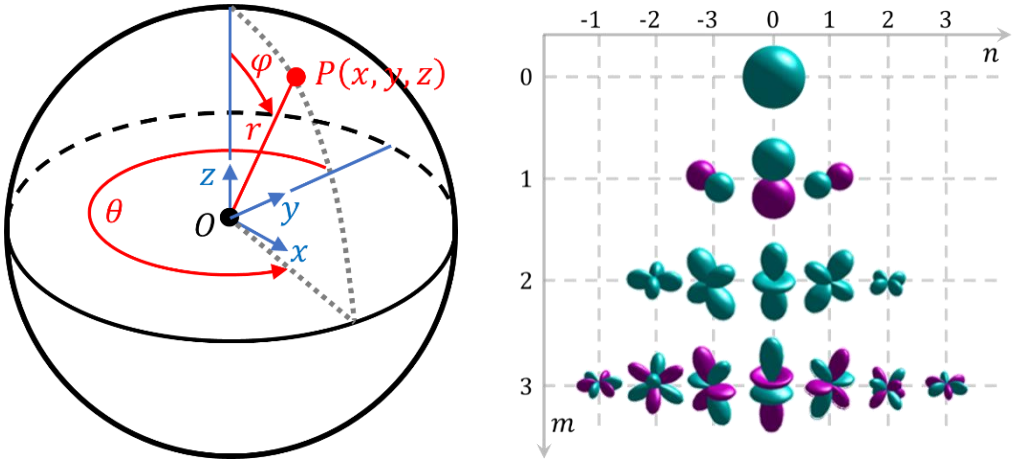

(a) (b)

Fig. 2 (a) The coordination transformation and (b) The first-order ($n = 0$) to the fourth-order ($n = 3$) of the harmonic basis function

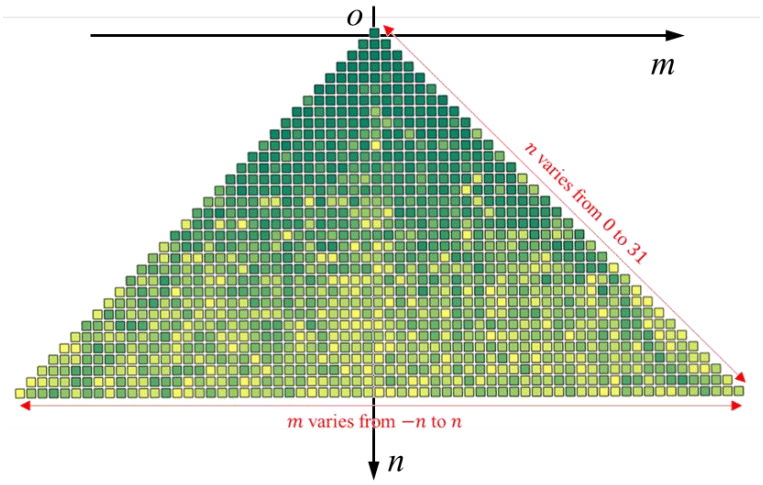

(*a*) Top view of the bar chart distribution for the harmonic coefficients

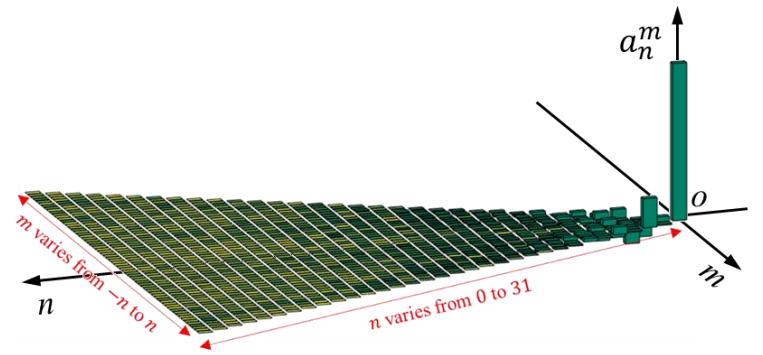

(*b*) Left view of the bar chart distribution for the harmonic coefficients

Fig. 3 The examples of harmonic coefficients

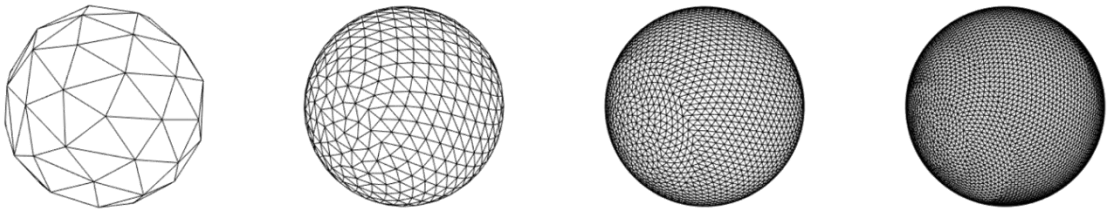

(*a*) (*b*) (*c*) (*d*)

Fig. 4 Illustration of uniformly distributed unit vertices with different N_P number

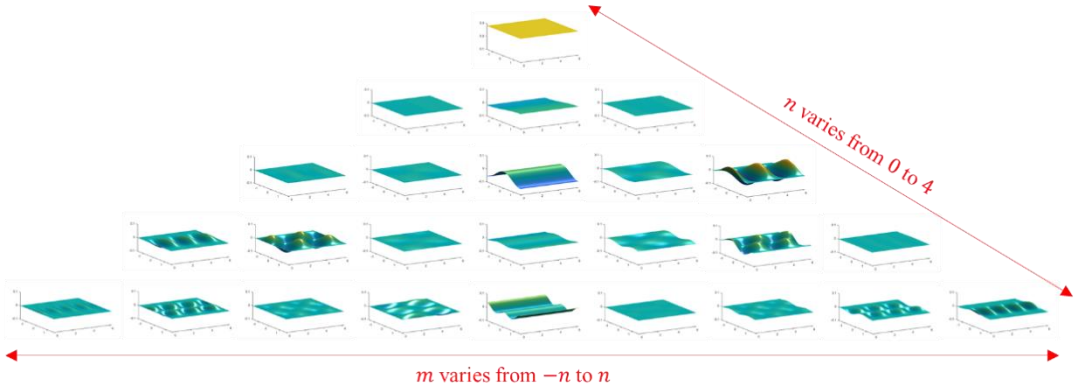

(*a*)

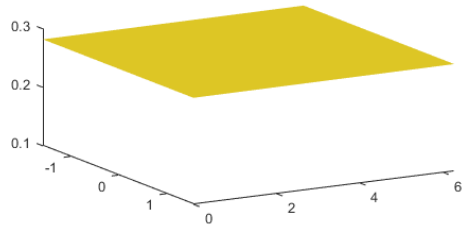

(*b*)

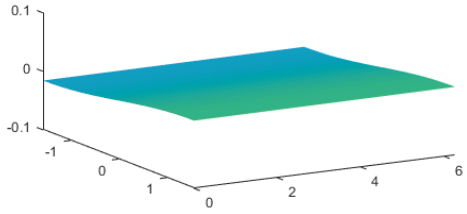

(*c*)

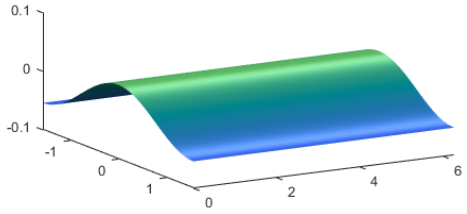

(*d*)

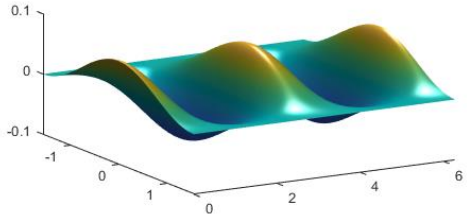

(*e*)

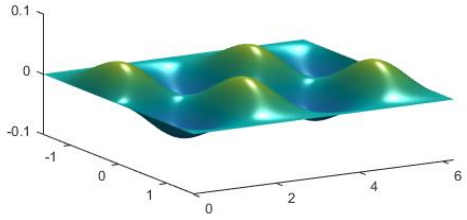

(*f*)

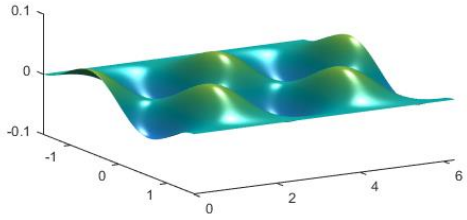

(*g*)

Fig. 5 The 3D contour map of $a_n^m Y_n^m(\theta, \varphi)$ for a specific pair of n and m

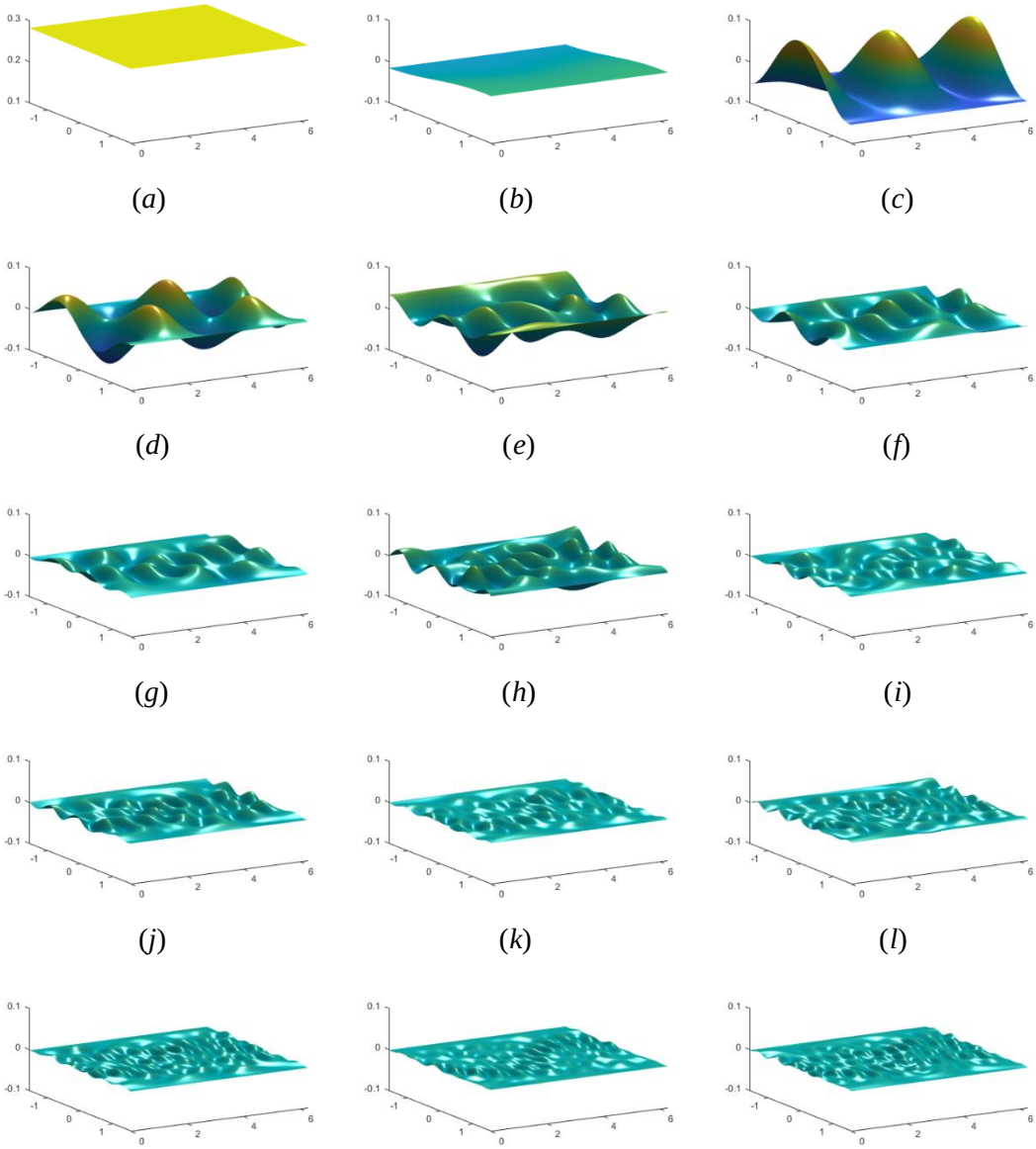

(*a*) (*b*) (*c*)

(*d*) (*e*) (*f*)

(*g*) (*h*) (*i*)

(*j*) (*k*) (*l*)

(*m*) (*n*) (*o*)

Fig. 6 Superimpose $a_n^m Y_n^m(\theta, \varphi)$ from $m = n$ to $m = -n$

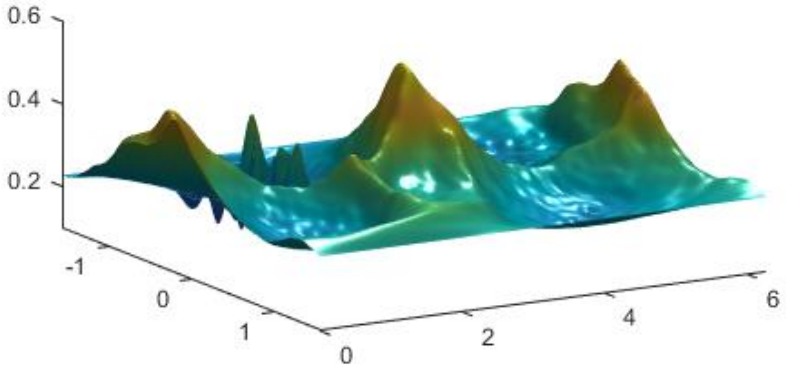

(a)

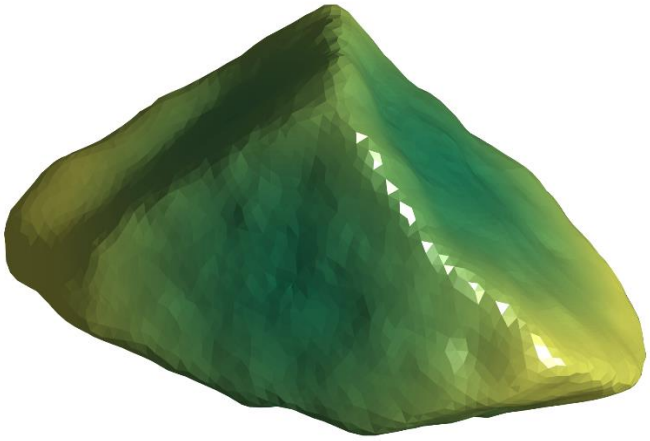

(b)

Fig. 7 (a) Superimpose $\sum a_n^m Y_n^m(\theta, \varphi)$ from $n = 1$ to $n = N$ and (b) Generated points cloud model that represents the target particle surface

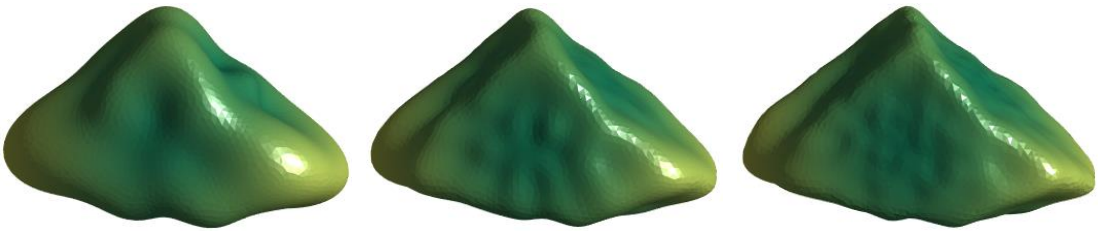

(*a*) (*b*) (*c*)

Fig. 8 Target particle surface represented by various harmonic orders

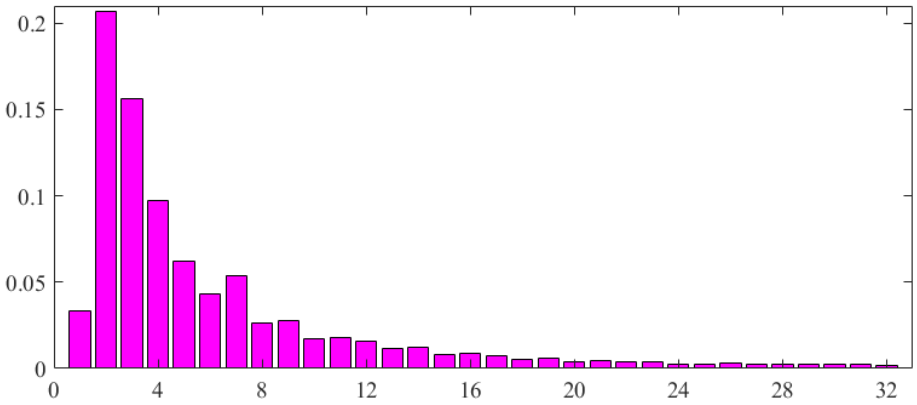

Fig. 9 Results of A_n for the example particle

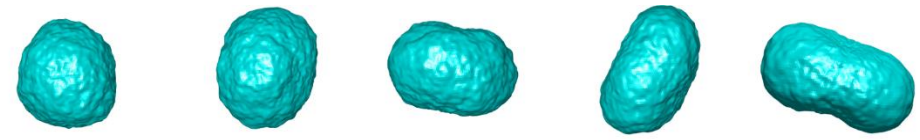

$A_2 = 0.00$ $A_2 = 0.05$ $A_2 = 0.10$ $A_2 = 0.15$ $A_2 = 0.20$

(a) A_2 vary from 0.00 to 0.20 while $A_3 = 0.03$ and $A_{16} = 0.005$

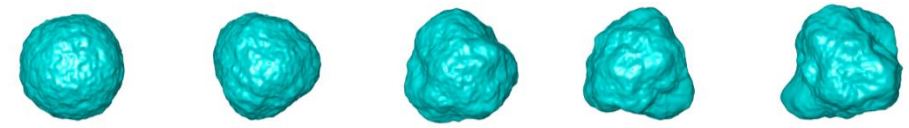

$A_3 = 0.02$ $A_3 = 0.04$ $A_3 = 0.06$ $A_3 = 0.08$ $A_3 = 0.10$

(b) A_3 vary from 0.02 to 0.10 while $A_2 = 0.0$ and $A_{16} = 0.005$

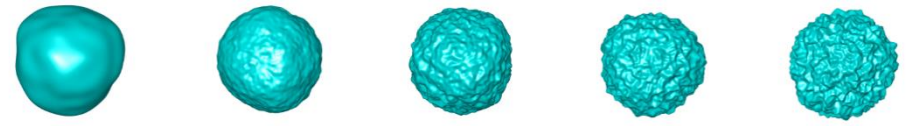

$A_{16} = 0.000$ $A_{16} = 0.004$ $A_{16} = 0.008$ $A_{16} = 0.012$ $A_{16} = 0.016$

(c) A_{16} varies from 0.000 to 0.016 while $A_2 = 0.0$ and $A_3 = 0.03$

Fig. 10 Generated virtual stone particles with different combinations of A_2, A_3 and A_{16}

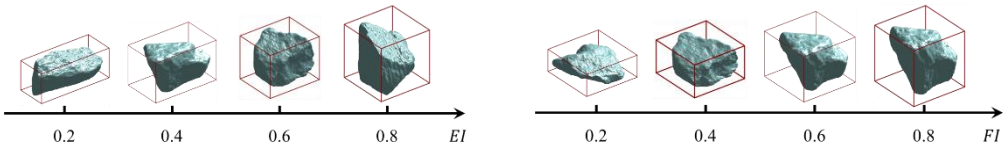

(*a*) (*b*)

Fig. 11 Examples of stone models with various values of EI and FI

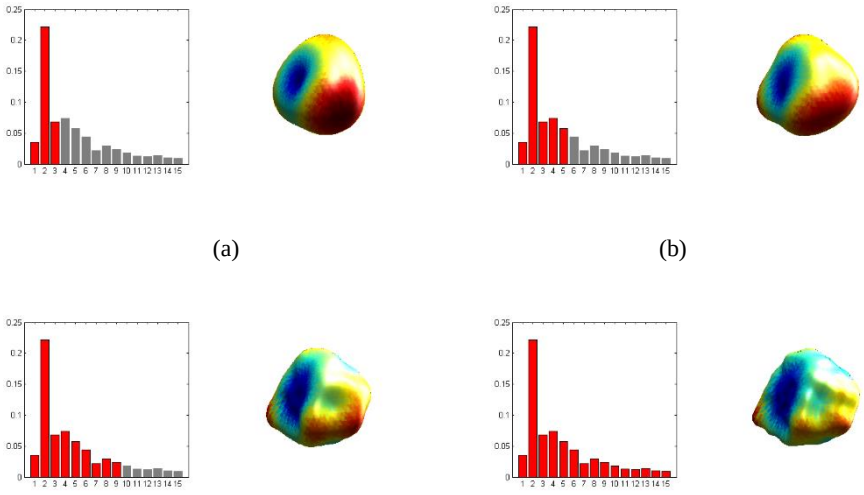

(a) (b)

(a) (b)

Fig. 12 Particle contour represented by different total order N

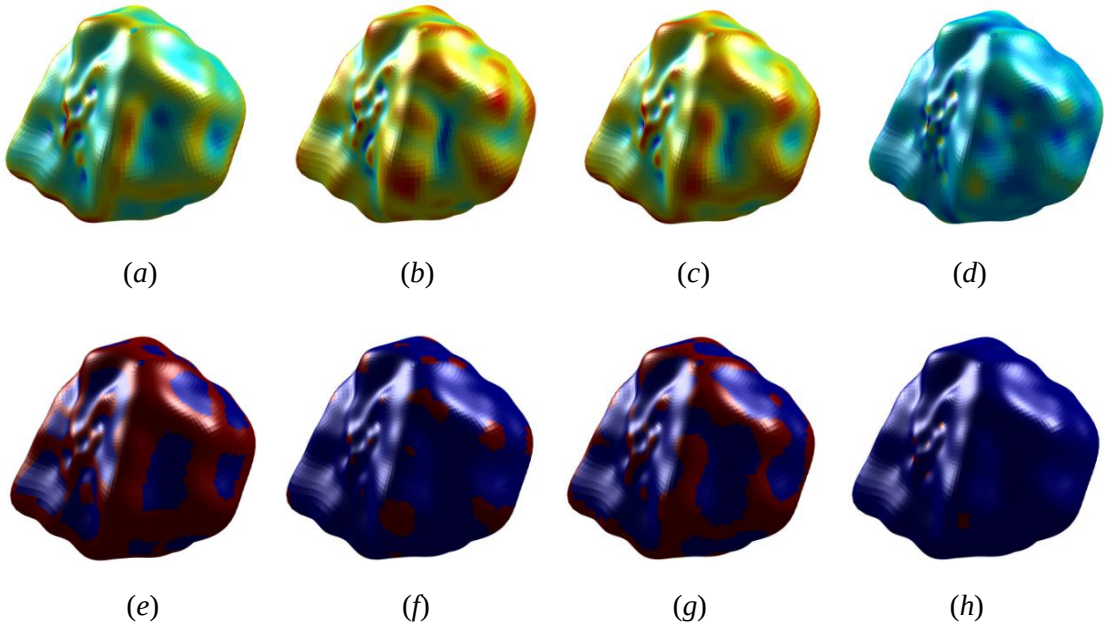

(*a*) (*b*) (*c*) (*d*)

(*e*) (*f*) (*g*) (*h*)

Fig. 13 The calculation effect diagram of local curvature

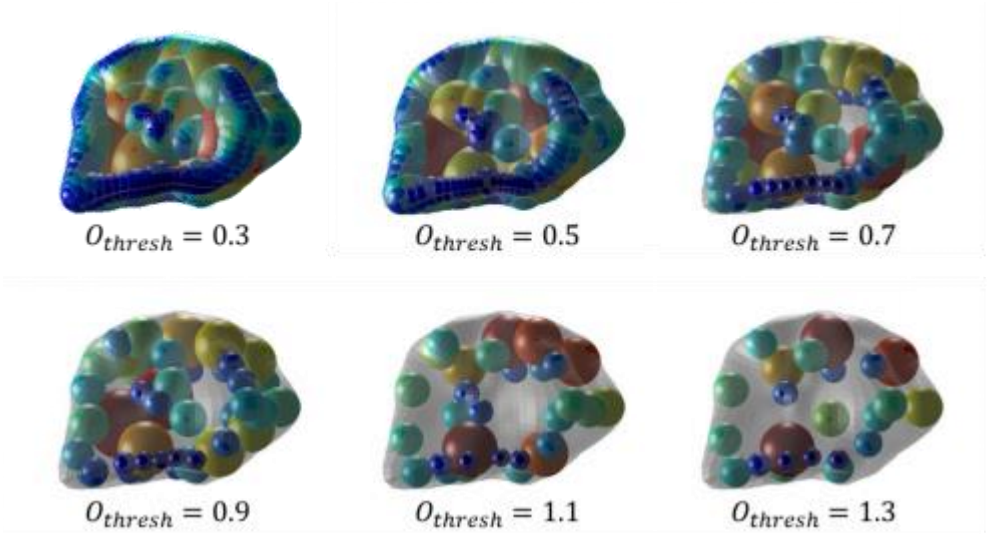

(*a*)

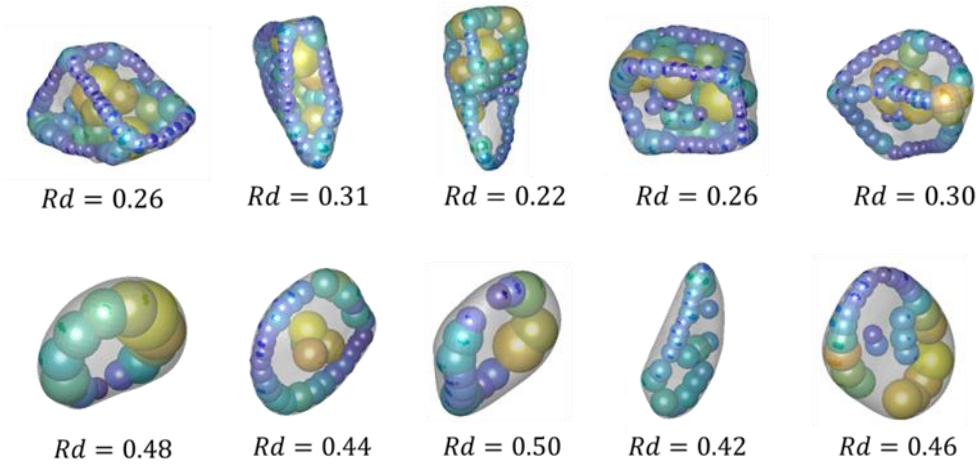

(*b*)

Fig. 14 (*a*) The effect of inscribed sphere in the corner area with different O_{thresh}; (*b*) Examples of stone particles with various values of Rd

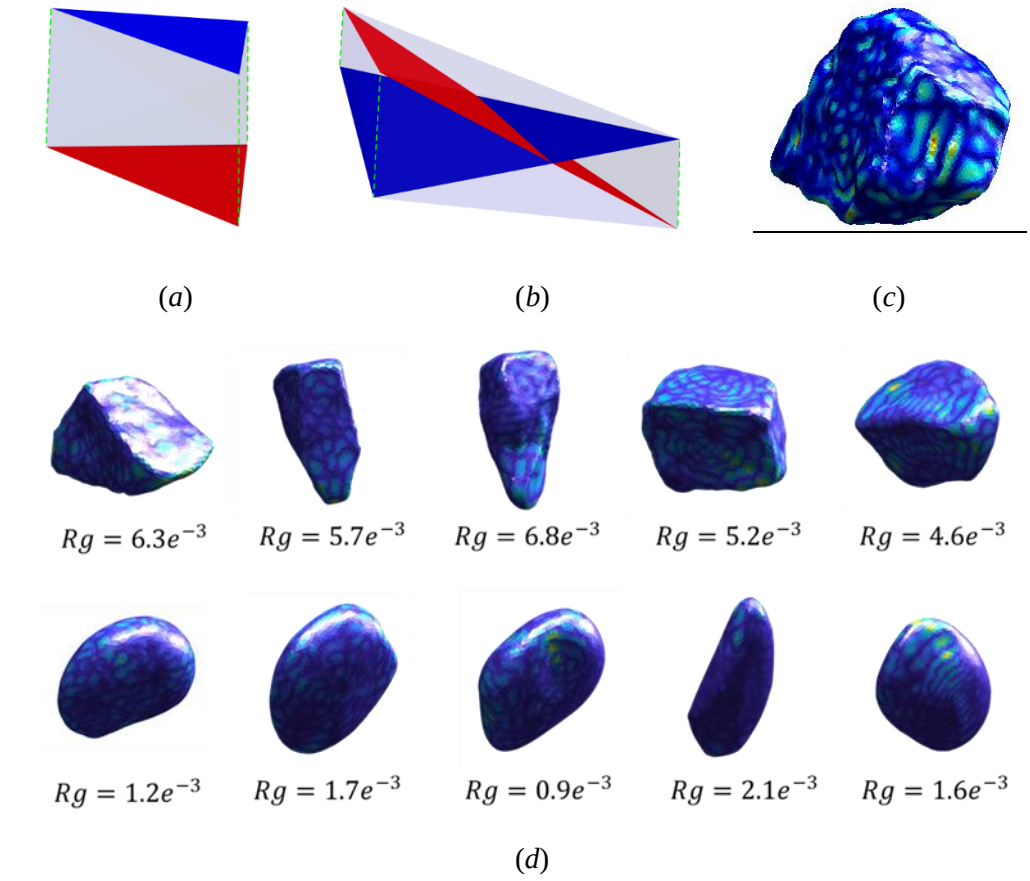

Fig. 15 Two conditions (*a*) and (*b*) to calculate local deviation distance, and (*c*) contour of local deviation distance; (*d*) Examples of stone particles with various values of Rg

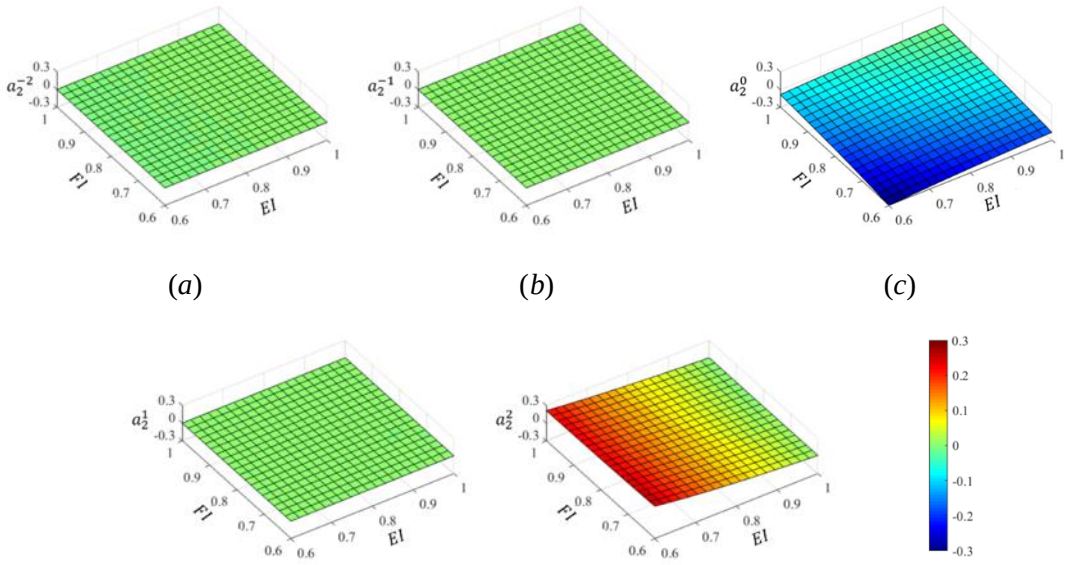

(*a*) (*b*) (*c*)

(*d*) (*e*)

Fig. 16 Evolution of (*a*) a_2^{-2}; (*b*) a_2^{-1}; (*c*) a_2^{0}; (*d*) a_2^{1}; (*e*) a_2^{2} versus EI_0 and FI_0

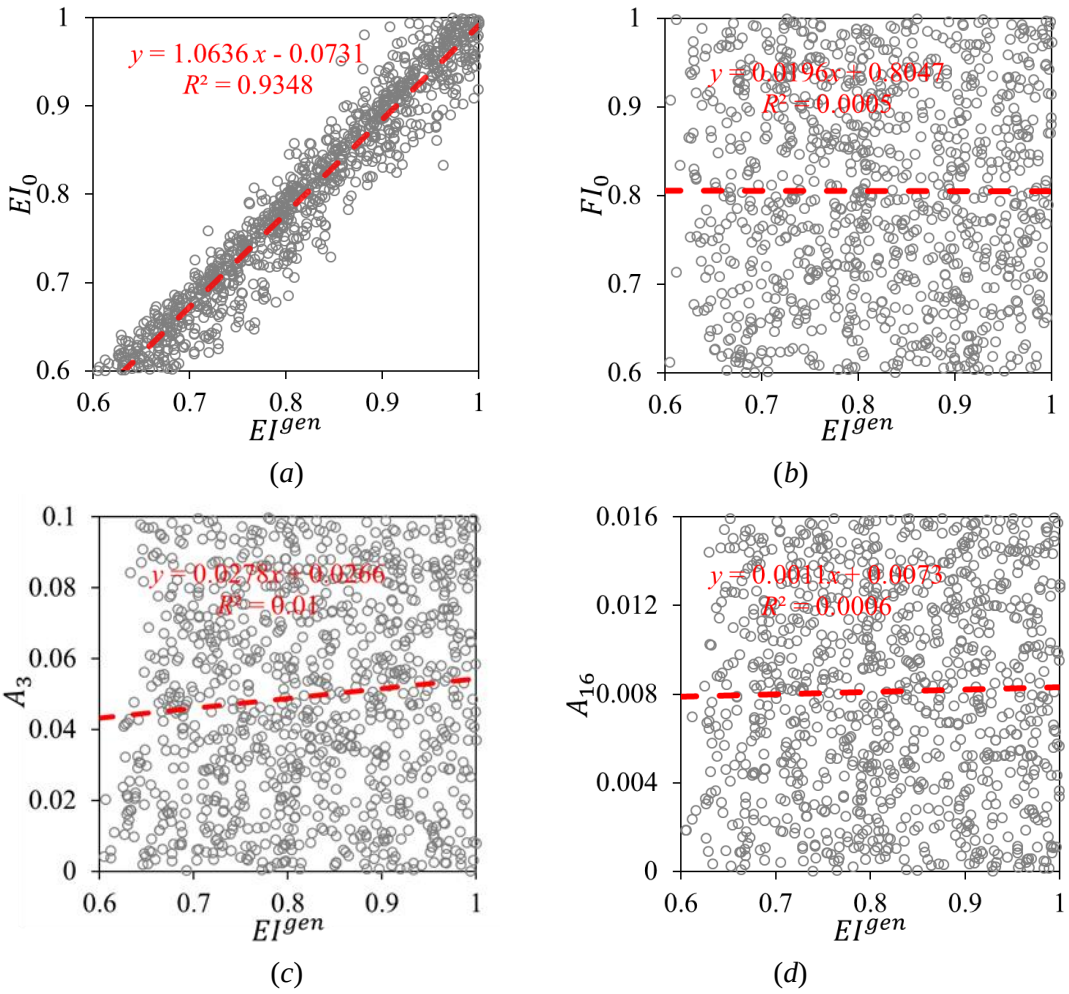

Fig. 17 The statistical relationships between EI^{gen} versus EI_0, FI_0, A_3 and A_{16}

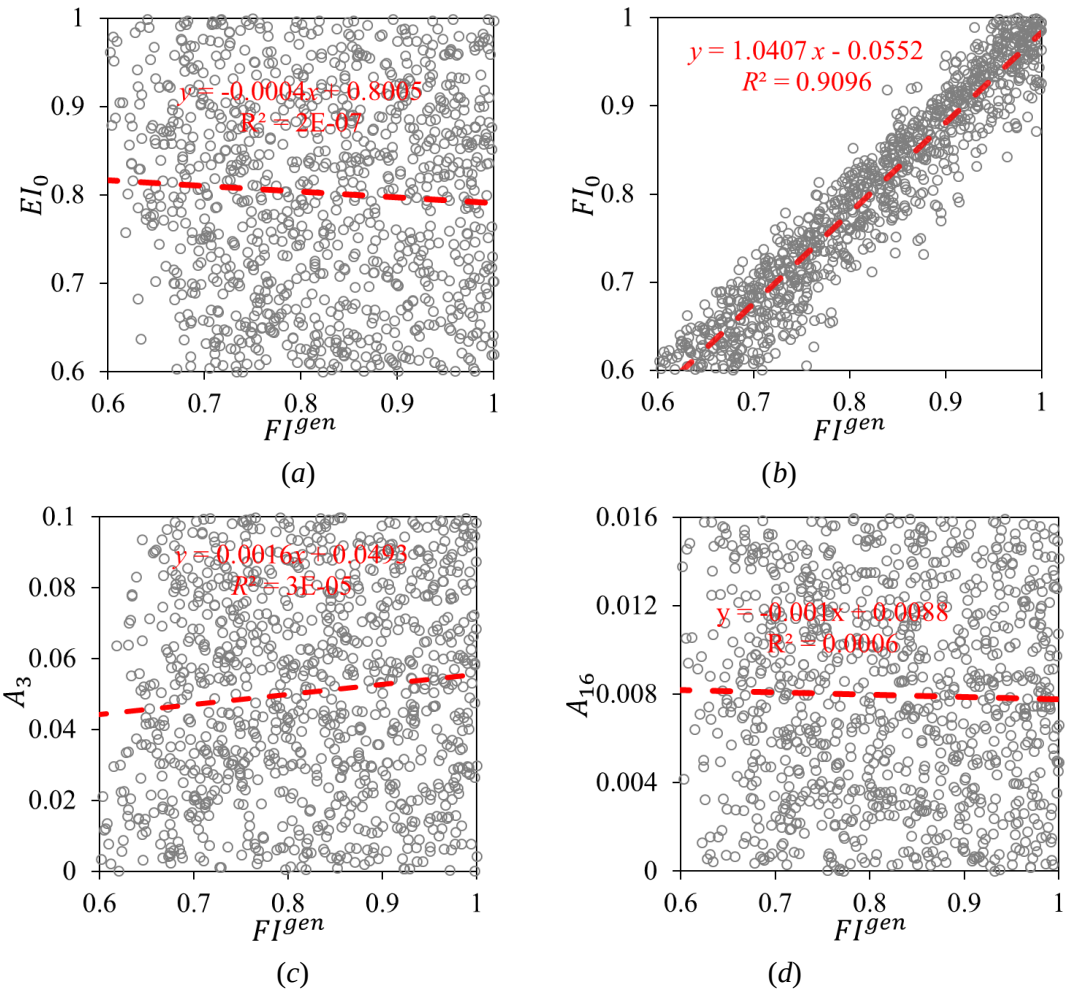

Fig. 18 The statistical relationships between FI^{gen} versus EI_0, FI_0, A_3 and A_{16}

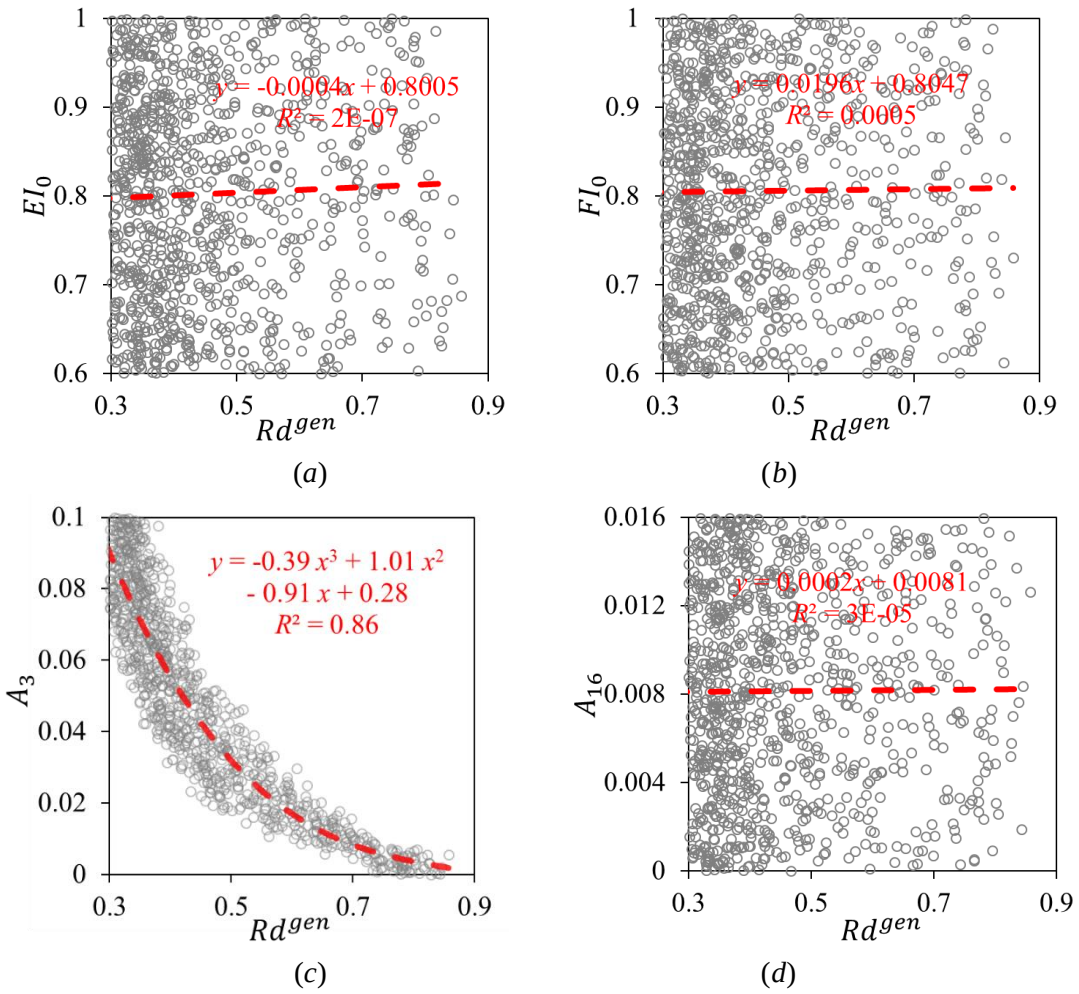

Fig. 19 The statistical relationships between Rd^{gen} versus EI_0, FI_0, A_3 and A_{16}

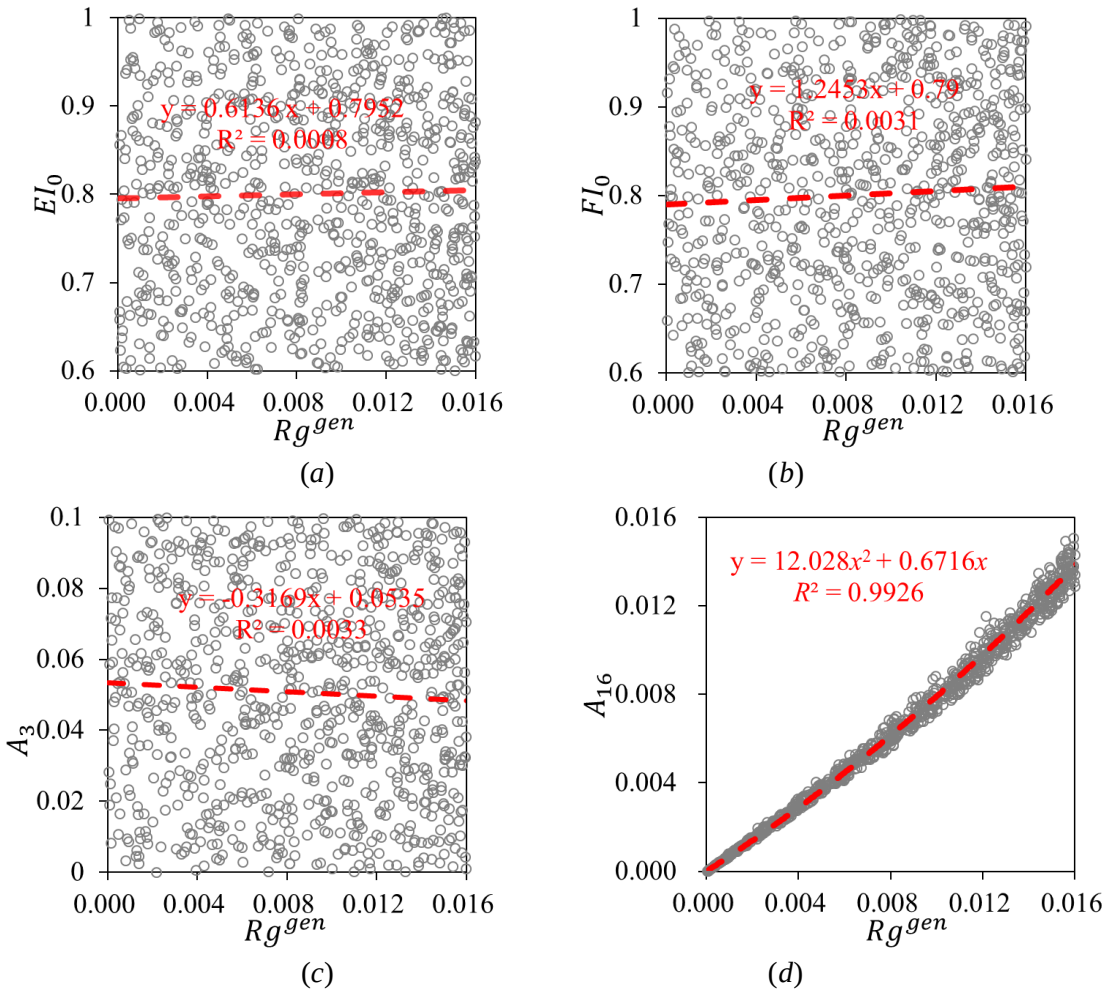

Fig. 20 The statistical relationships between Rd^{gen} versus EI_0, FI_0, A_3 and A_{16}

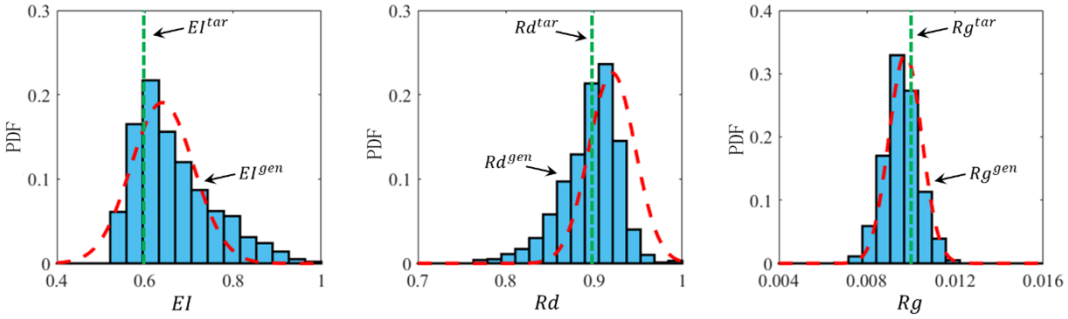

(*a*) (*b*) (*c*)

Fig. 21 The statistical distributions of generated particle shapes

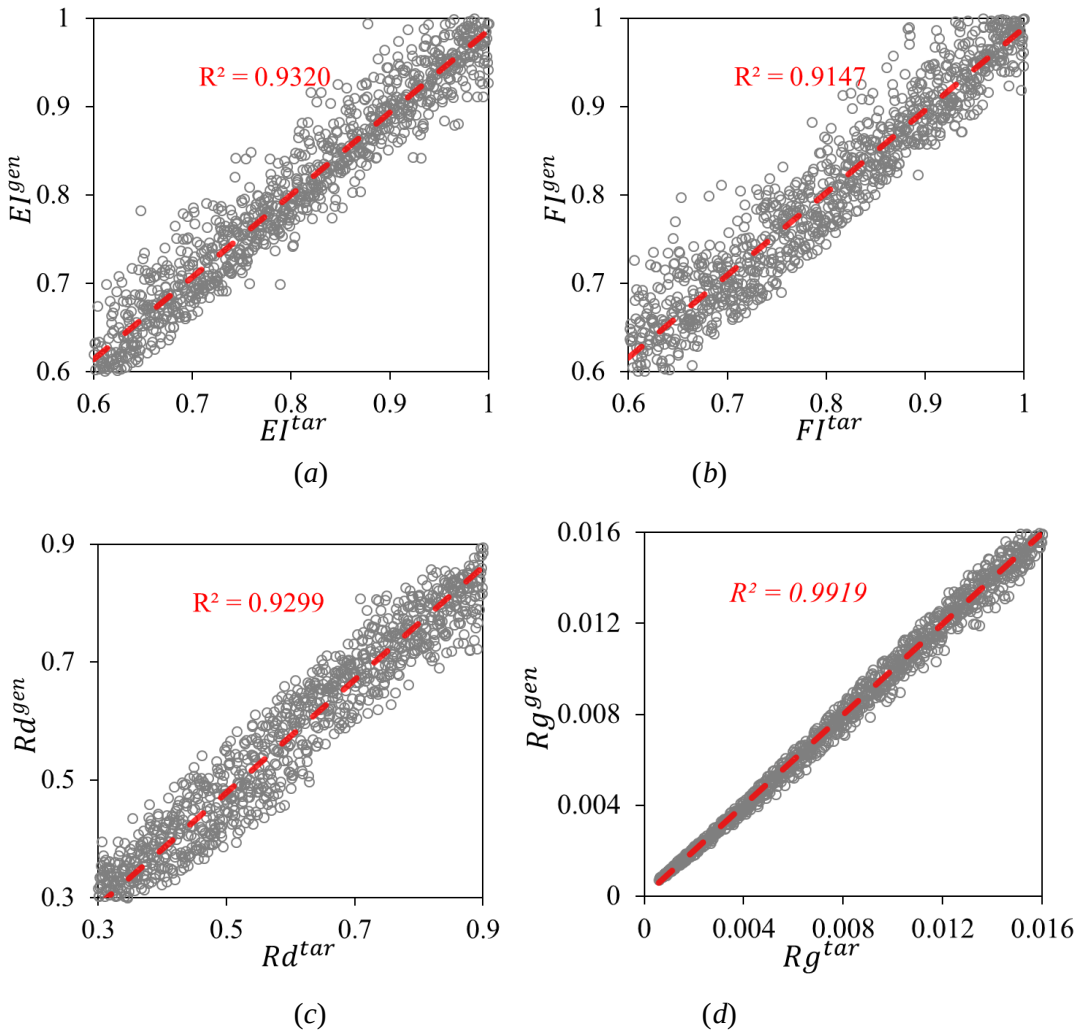

Fig. 22 The relation between EI^{tar}, FI^{tar}, Rd^{tar} and Rg^{tar} versus EI^{gen}, FI^{gen}, Rd^{gen} and Rg^{gen}

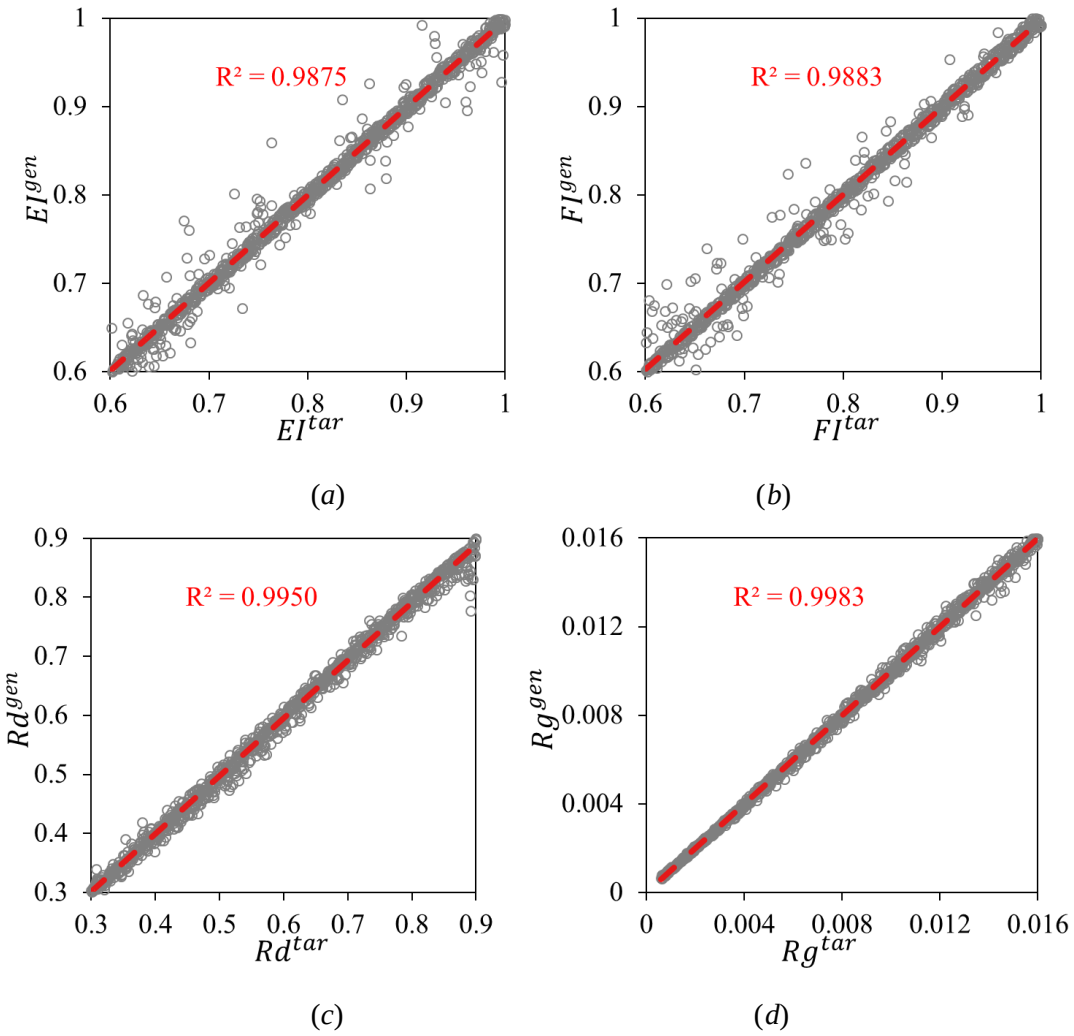

Fig. 23 The relation between EI^{tar}, FI^{tar}, Rd^{tar} and Rg^{tar} versus EI^{gen}, FI^{gen}, Rd^{gen} and Rg^{gen} after processed by inverse Monte Carlo algorithm

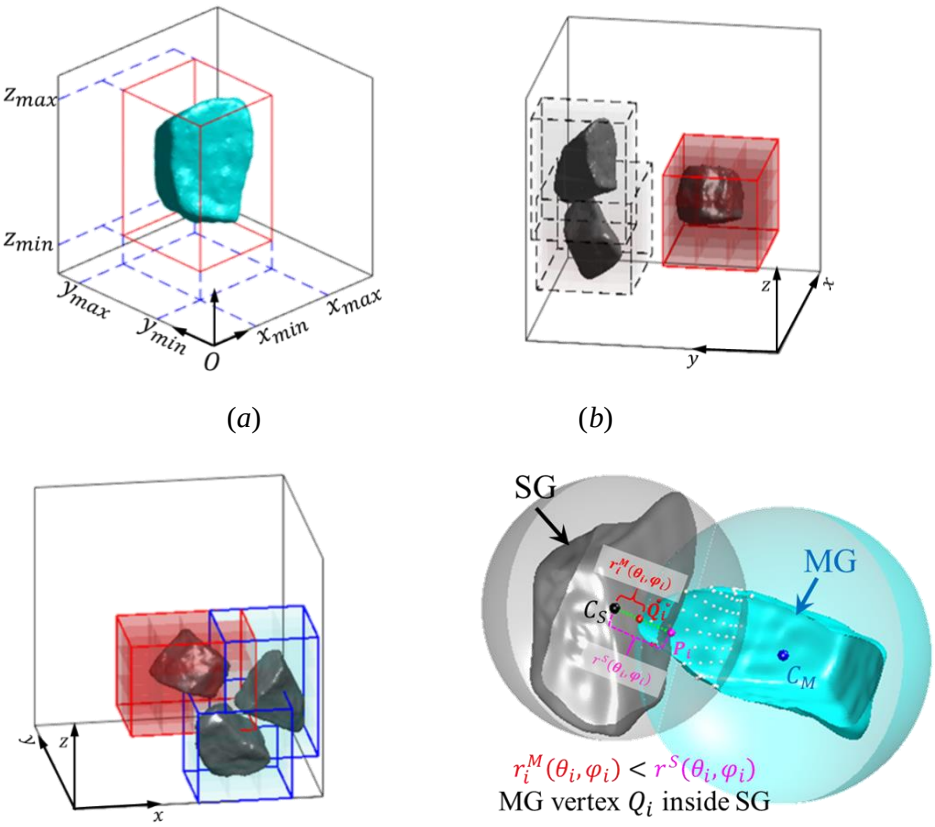

Fig. 24 (*a*) AABB of an example particle in the global Cartesian coordinate system, (*b*) non-overlapping condition; (*c*) potential overlapping condition and (*d*) identification of penetration condition

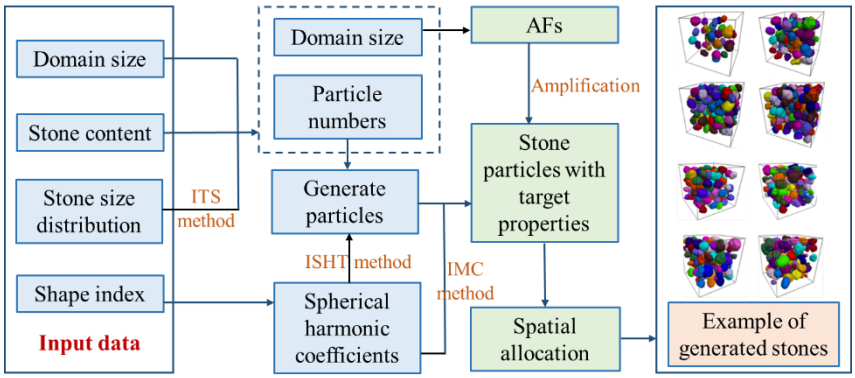

Fig. 25 The workflow to generate numerical model of desired stone sample

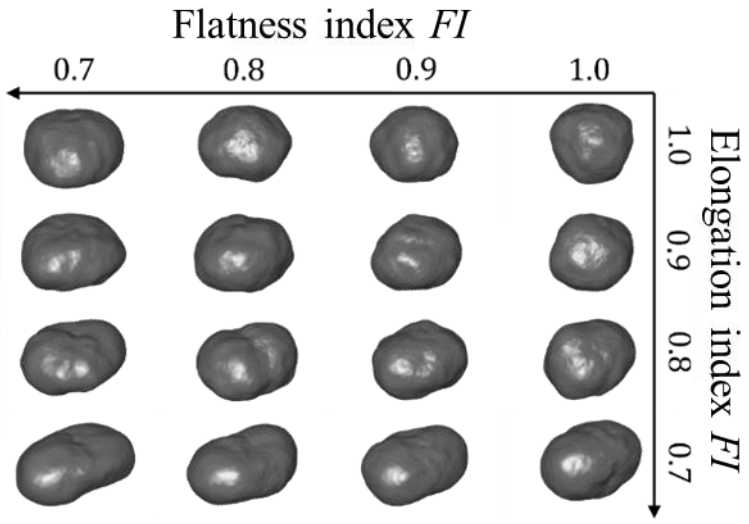

(*a*)

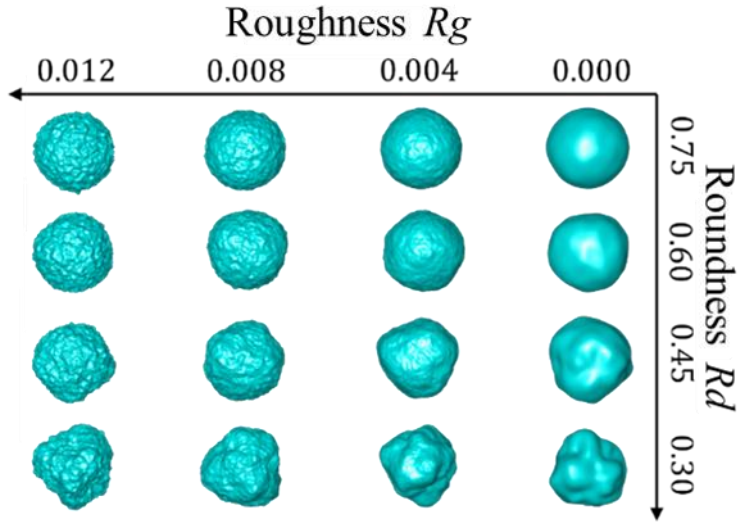

(*b*)

Fig. 26 (a) Cobble-like particle with various elongation and flatness; and (b) Equant particle with various roughness and roundness

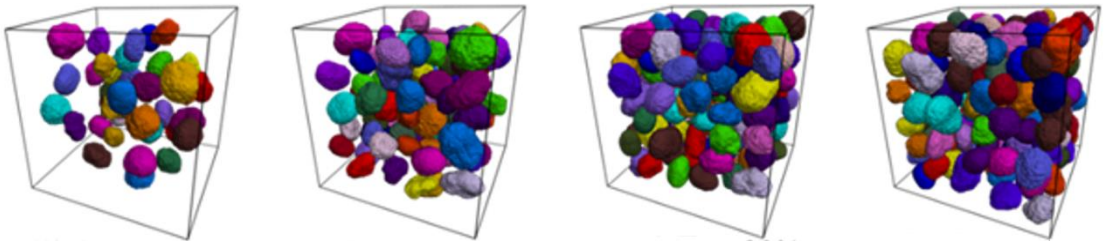

(*a*) stone-based material models with various stone contents

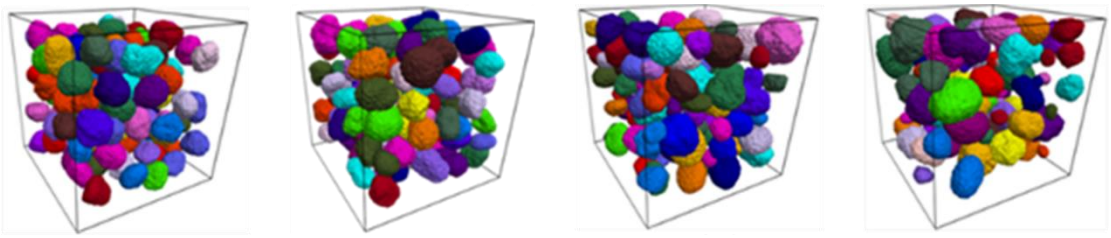

(*b*) stone-based material models with various stone gradations

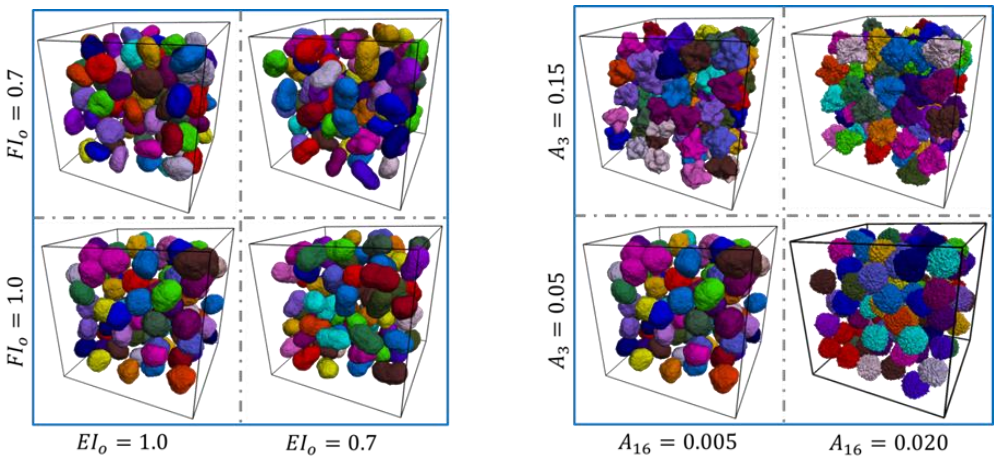

(*c*) stone-based material models with various stone shapes

Fig. 27 Geometry-controlled generation of stone-based material models

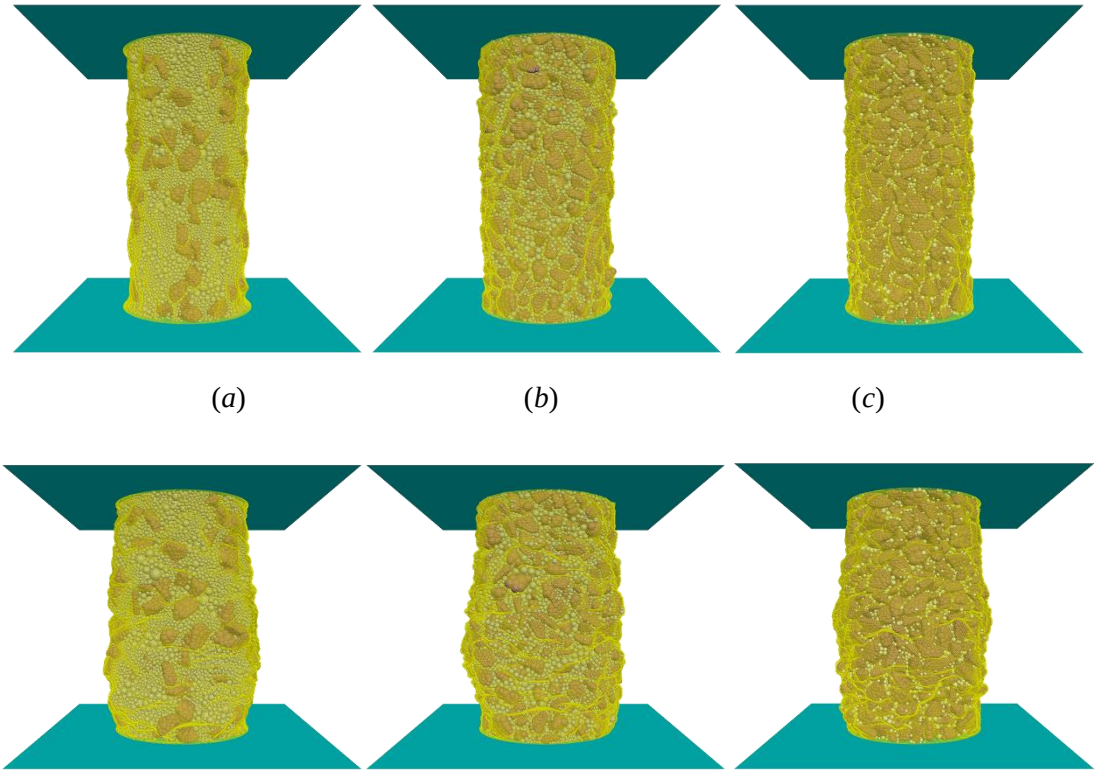

(*a*) (*b*) (*c*)

(*d*) (*e*) (*f*)

Fig. 28 Examples of preshear numerical models and the numerical models at the shear strain of 15%

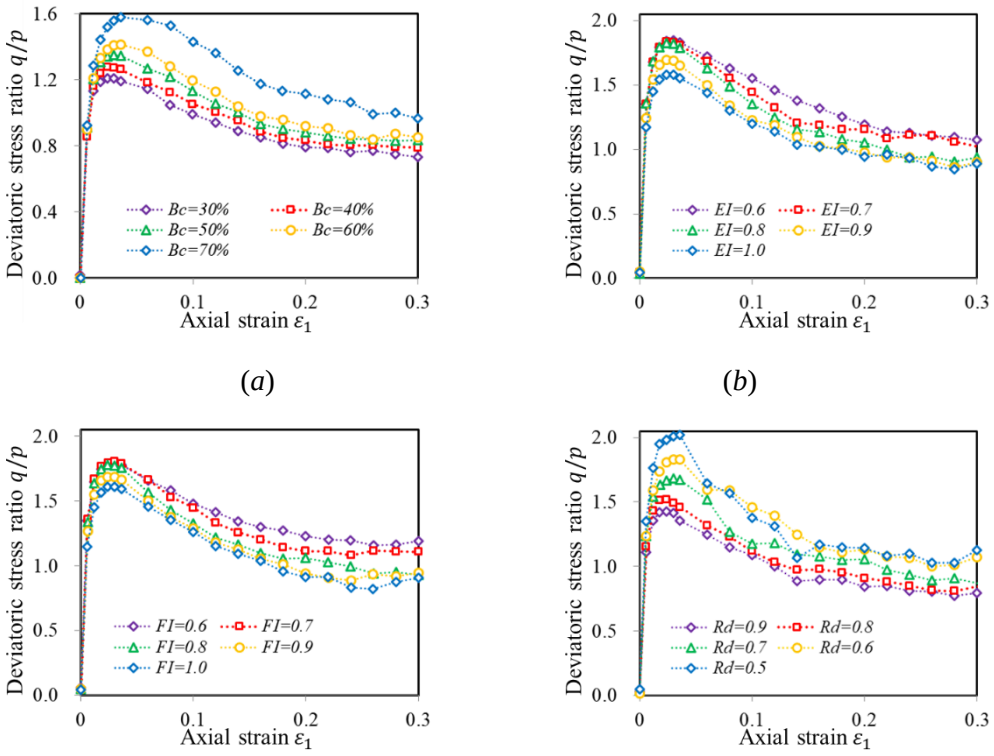

Fig. 29 The evolution of deviator stress ratio η versus axial strain ε_1 for stone-based material with (a) different stone content, (b) different elongation index, (c) different flatness idenx, and (d) roundness shape

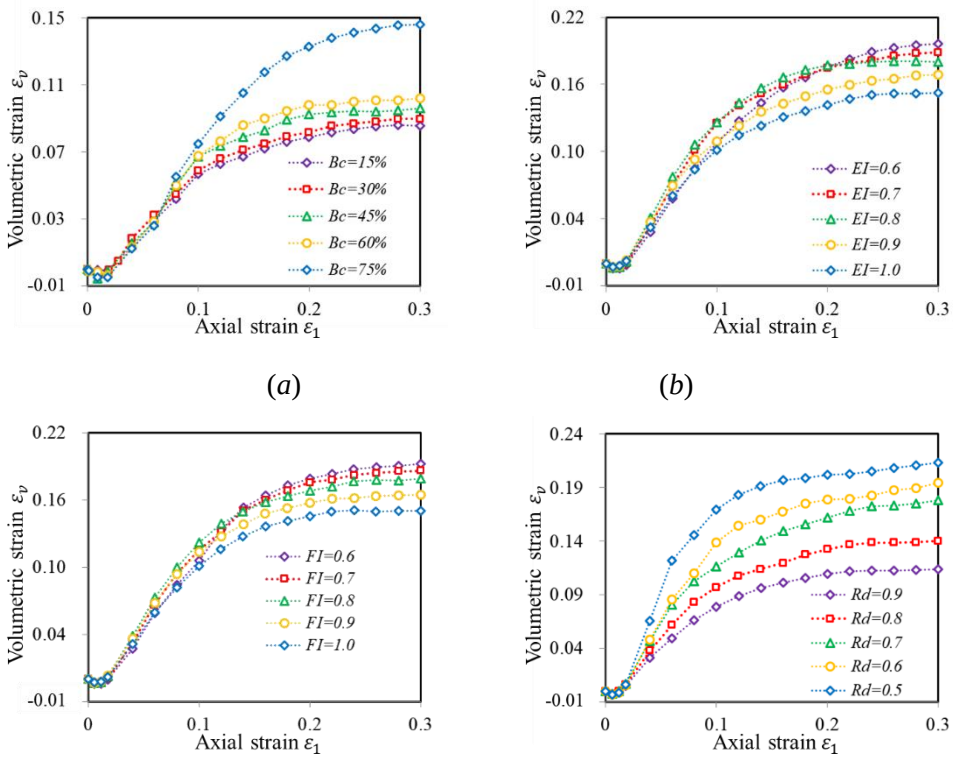

Fig. 30 The evolution of volumetric strain ε_v versus axial strain ε_1 for stone-based material with (a) different stone content, (b) different elongation index, (c) different flatness idenx, and (d) roundness shape

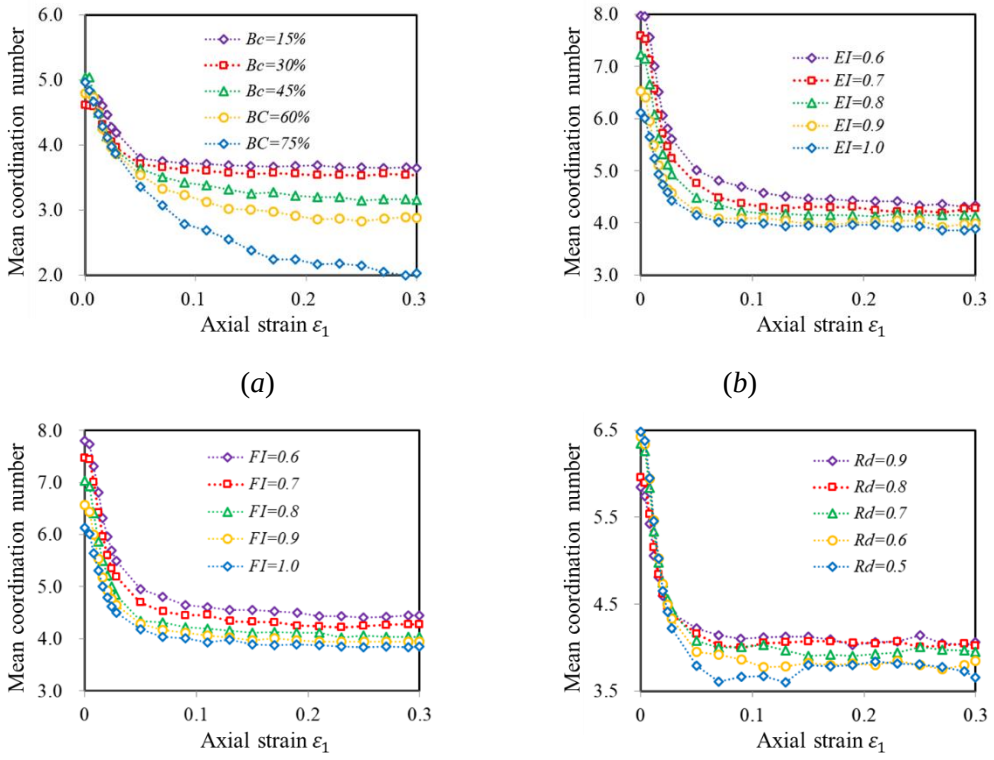

Fig. 31 The evolution of mean coordination number Z versus axial strain ε_1 for different groups

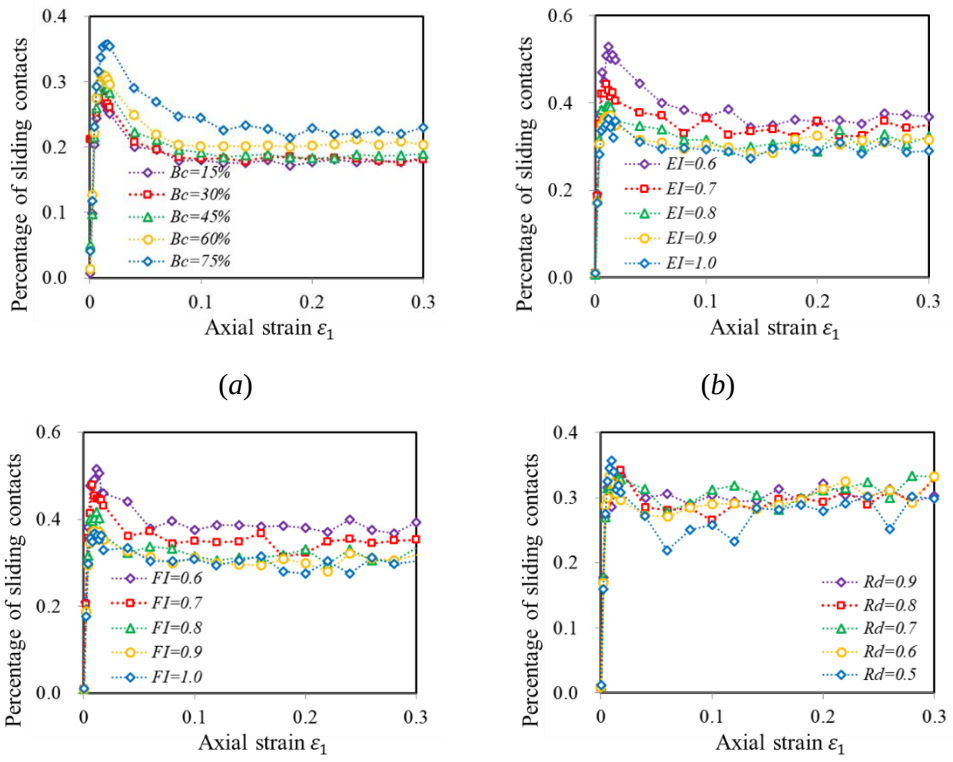

(*a*) (*b*)

(*c*) (*d*)

Fig. 32 The evolution of percentage of sliding contact versus axial strain ε_1 for different groups